Mediator Subunit Med4 Enforces Metastatic Dormancy in Breast Cancer

Authors:
Seong-Yeon Bae[1-4*], Hsiang-Hsi Ling[1-4], Yi Chen[2,5-6], Hong Chen[3,7], Dhiraj Kumar[1-3], Jiankang Zhang[1-4], Aaron D. Viny[2, 4-6], Ronald A. DePinho[3*], Filippo G. Giancotti[1-4†]

Affiliations:

[1]Cancer Metastasis Initiative, Herbert Irving Comprehensive Cancer Center, Columbia University Irving Medical Center, New York, New York 10032, USA
[2]Department of Genetics and Development, Vagelos College of Physicians and Surgeons, Columbia University Irving Medical Center, New York, New York 10032, USA
[3]Department of Cancer Biology, The University of Texas MD Anderson Cancer Center, Houston, Texas 77054, USA
[4]Herbert Irving Comprehensive Cancer Center, Columbia University Irving Medical Center, New York, New York 10032, USA
[5]Columbia Stem Cell Initiative, Vagelos College of Physicians and Surgeons, Columbia University Irving Medical Center, New York, New York 10032, USA
[6]Division of Hematology and Oncology, Department of Medicine, Columbia University Irving Medical Center, New York, New York 10032, USA
[7]Department of Thoracic/Head and Neck Medical Oncology, The University of Texas MD Anderson Cancer Center, Houston, Texas 77054, USA
[†]Deceased

*Correspondence: sb4595@cumc.columbia.edu (S.-Y.B.), RDePinho@mdanderson.org (R.A.D)

Summary

Long term survival of breast cancer patients is limited due to recurrence from metastatic dormant cancer cells. However, the mechanisms by which these dormant breast cancer cells survive and awaken remain poorly understood. Our unbiased genome-scale genetic screen in mice identified *Med4* as a novel cancer-cell intrinsic gatekeeper in metastatic reactivation. *MED4* haploinsufficiency is prevalent in metastatic breast cancer patients and correlates with poorer prognosis. Syngeneic xenograft models revealed that *Med4* enforces breast cancer dormancy. Contrary to the canonical function of the Mediator complex in activating gene expression, *Med4* maintains 3D chromatin compaction and enhancer landscape, by preventing enhancer priming or activation through the suppression of H3K4me1 deposition. *Med4* haploinsufficiency disrupts enhancer poise and reprograms the enhancer dynamics to facilitate extracellular matrix (ECM) gene expression and integrin-mediated mechano-transduction, driving metastatic growth. Our findings establish *Med4* as a key regulator of cellular dormancy and a potential biomarker for high-risk metastatic relapse.

Keywords: breast cancer, dormancy, metastasis, Mediator complex, enhancer, extracellular matrix

Introduction

Survivorship for patients with breast cancer is predicated not by the disease burden in the breast itself, but rather the ability of cancer cells to metastasize outside the breast. Clinical experience and experimental data in both patients and mouse models show that metastatic disease is the overwhelming cause of breast cancer deaths. Cellular and molecular studies of metastatic breast cancer suggest that disseminating cells from the primary tumor undergo a variable period of dormancy at pre-metastatic sites before undergoing reactivation and outgrowth becoming macroscopic and life-threatening lesions(Early Breast Cancer Trialists' Collaborative, 2005). These data point to a distinct stage of tumor progression whereby quiescence may serve as both a biomarker of high-risk disease as well as a key therapeutic target. We posit that cancer cell dormancy within the early metastatic niche provides a therapeutic window of opportunity across breast cancer subtypes including triple-negative breast cancer (TNBC), despite its historically perceived short clinical latency(Giancotti, 2013; Zhang et al., 2013),with a subgroup of TNBC patients exhibiting recurrence after five years(Rueda et al., 2019).

Genomic studies of breast cancer growth kinetics have indicated that systemic spread can occur rapidly following malignant transformation(Hosseini et al., 2016; Hu et al., 2020; Turajlic and Swanton, 2016; Werner-Klein et al., 2020). Early disseminated cancer cells (DCCs) often lack critical genetic and genomic alterations, which they need to acquire at distant sites. This suggests that their outgrowth in target organs may be driven by epigenetic mechanisms regulating key features of cellular identity, such as epithelial-to-mesenchymal transition (EMT) and stemness/self-renewal(Lambert et al., 2017). Indeed, analysis of metastasis driver genes through gene ontology has revealed enrichment for chromatin regulators in metastatic progression(Hu et al., 2020). Despite their clinical importance, metastatic dormancy and reactivation are poorly understood due to the complexity of the underlying biology. To untangle this complexity, we developed a forward genetic screening strategy in the mouse to uncover key regulators of metastatic reactivation(Gao et al., 2014). Screening of open reading frame (ORF) libraries enabled us to identify several positive regulators of metastatic reactivation of breast cancer, including Coco, which binds to and inhibits BMP in the lung microenvironment, and the tetraspanin family member

TM4SF1, which mediates non-canonical activation of the JAK2-STAT3 signaling pathway(Gao et al., 2012; Gao et al., 2016).

Collectively, our prior studies suggest that metastatic outgrowth is initiated by a subpopulation of cancer stem cells with metastatic potential (metastasis-initiating cells), which undergo dormancy and reactivation in response to then activation of signaling pathways and transcriptional networks similar to those that govern these processes in adult stem cells(Giancotti, 2013). However, numerous modulators involved in regulating metastatic dormancy remain to be identified due to the extensive heterogeneity observed in the molecular, genetic, and clinical characteristics of breast cancer metastases. To identify additional modulators associated with metastatic dormancy, we conducted an *in vivo* CRISPR-Cas9 screen aimed at identifying genetic factors that contribute to breast cancer reactivation in DCCs. Here we demonstrate *mediator complex subunit 4* (*Med4*) as a novel cancer cell intrinsic gatekeeper in metastatic reactivation.

The Mediator complex regulates Pol II-mediated transcription by adjoining enhancer-bound transcription factors and the general transcription machinery in *cis*(El Khattabi et al., 2019; Whyte et al., 2013). Mediator, comprising a 26-subunit core organized into head, middle, and tail modules, and a four-subunit dissociable kinase module, manifests functional adaptability due to the variable arrangement of its subunits(Abdella et al., 2021; Verger et al., 2019). The subunit-specific composition and function of Mediator in its interaction with transcription factors (TF) imply that individual subunits of the complex regulate distinct transcriptional responses(Allen and Taatjes, 2015; Soutourina, 2018). The molecular basis for the disparate functional roles of individual subunits in various biological contexts remains incompletely understood(Barbieri et al., 2012; Ito et al., 2000; Stevens et al., 2002), particularly as it pertains to *Med4*. We show that genetic perturbation of *Med4* awakens dormant tumor cells in pre-metastatic niches. The clinical relevance of our findings is supported by the observation that low *MED4* expression is associated with increased risk of metastatic relapse in patients with breast cancer. Taken together, we propose a novel epigenetic regulatory mechanism whereby *Med4* depletion rewires integrin signaling through decompaction of 3-dimensional chromatin architecture and enhancer reprogramming.

Results

Genome-scale CRISPR KO screen identifies *Med4* as a dormancy regulator.

To identify novel regulators enforcing breast cancer dormancy, we performed a genome-wide CRISPR knockout (KO) screen using the GeCKO v2 library containing 67,405 sgRNAs that was designed to target 20,611 distinct genes in the mouse genome (Gao et al., 2014; Joung et al., 2017) (Figure 1A). Following tail vein injection and lung infiltration, 4T07 breast cancer cells acquired the ability to exit dormancy, underwent reactivation and generated macrometastases (Figure S1A). After isolating tumor cells from each lung metastasis, we cloned and performed Sanger sequencing on the integrated sgRNA inserts to identify single genes that can reactivate metastasis and identified 26 unique metastases associated with a single sgRNA, which was discernible through Sanger sequencing (Table S1). Intriguingly, we identified sgRNAs targeting 3 genes (*Med4*, *Nipbl; Nipped-B-like protein*, and *Esco1; Establishment of sister chromatid cohesion N-acetyltransferase 1*) involved in the formation of super-enhancers among the top 3 hits from the initial validation. Whereas MED4 is a core subunit of the Mediator complex, which connects super-enhancers and promoters in *cis*, NIPBL and ESCO1 aid in loading cohesin onto DNA and hence physically stabilize the assembly of the super-enhancer-promoter complex (Figure S1B). We further

examined the effects of knocking down each gene using multiple shRNAs in both 4T07-TGL and D2A1-d-TGL cells. *Med4* emerged as the most promising hit, showing biological potency across three different shRNAs and in both cell lines. (Figure 1B).

To confirm that the *Med4* gene was genuinely edited to promote metastasis, we performed indel PCR analysis and western blotting in the clone originally isolated from the screen. The results indicated that the clone which contains a sgRNA targeting *Med4*, carried heterozygous instead of homozygous deletion (one allele of the clone carries a nonsense mutation) (Figure S1C-S1F). We hypothesized that *Med4* is an essential gene with examination of the DepMap database supports dependency on *Med4* (Figure S1G)(Tsherniak et al., 2017). In agreement with the essentiality of *Med4*, we were not able to generate *Med4* KO clones presumably because of strong counterselection. Hereafter, we focused on *Med4* due to its strong selection in our genome-scale screen, its potent metastatic modulatory activity *in vivo*, its central role in gene transcriptional regulation, its genomic alteration in human breast cancer metastases (see below), and its unexplored role in governing metastatic dormancy.

Med4 enforces dormancy.

To validate the biological potency of *Med4 in vivo*, we used MirE shRNA to target *Med4* in 4T07-TGL cells (Figure S1H-S1I) and another model for breast cancer dormancy, D2A1-d-TGL cells (Figure 1C-1F). Upon *Med4* silencing, the cancer cells acquired the capacity to efficiently colonize the lung when intravenously injected into immunocompetent mice. To determine if *Med4* silencing specifically induces reactivation from dormancy in early metastatic niches, we used a doxycycline-inducible promoter to express shRNAs targeting *Med4*. Mice were treated with doxycycline either immediately or 2 weeks after tail vein injection (Figure 1G). Whereas immediate knockdown of *Med4* induced metastatic outgrowth at around 2 weeks, a 2-week delay in *Med4* knockdown caused a similar delay in metastatic outgrowth (Figure 1H-1J), confirming that *Med4* downregulation re-awakens breast cancer cells from dormancy. Clinically, breast exhibits a propensity for metastasis to distinct organs, including the lungs, bones, brain, and liver(Obenauf and Massague, 2015). To assess the impact of *Med4* depletion on promoting colonization in other organs, we systemically administered cancer cells by injecting them into the left ventricle. While control cells remained dormant after 4 weeks, *Med4*-depleted cells exhibited a diffuse whole-body bioluminescence signal (Figure 1K). Subsequent dissection and *ex vivo* bioluminescence analysis revealed that metastases were exclusive to the bone following left ventricle inoculation, particularly in the epiphysis of the femur, tibia, and humerus (Figure 1L). Histological examination using H&E staining confirmed the presence of cancer cells within the epiphysis, along with associated bone lesions. Further analysis by TRAP staining identified the presence of osteoclasts near the lesions, indicative of osteolytic metastasis (Figure 1M). Taken together, these findings suggest that *Med4* maintains dormancy in breast cancer.

Med4 preserves the transcriptional and epigenetic landscape, preventing the formation of desmoplastic niches.

To obtain a comprehensive view of the transcriptional reprograming in dormancy and metastatic reactivation, we performed bulk RNA sequencing (RNA-seq) of D2A1 (metastatic) cells and its dormant variant D2A1-d cells(De Cock et al., 2016). We identified a D2A1_metastatic gene signature (225 differentially upregulated genes in D2A1) and a D2A1_dormant gene signature (207 differentially upregulated genes in D2A1-d) (Figure S2A). We employed both signatures in

153 analyzing bulk RNA-seq data from D2A1-d cells expressing two different shRNAs targeting *Med4*,
154 in comparison to a control shRNA. Gene set enrichment analysis (GSEA) indicates that the
155 D2A1_metastatic signature was enriched in *Med4*-silenced cells while the D2A1_dormant
156 signature was enriched in control cells (Figure S2B). These results indicate that *Med4* depletion
157 reprograms transcriptional profile from a dormant to a metastatic state. In addition, RNA-seq
158 revealed that *Med4* silencing skews the transcriptomic profiles towards upregulation of gene
159 expression, in contrast to the well-known function of the Mediator complex in
160 transcription(Soutourina, 2018) (Figure 2A; Table S2-S5). To determine if the changes in the
161 transcriptome resulting from *Med4* silencing are a general feature of the Mediator complex or
162 specific to *Med4*, we employed MirE shRNA to target the Mediator complex subunit 1 (*Med1*)
163 (Figure S2C). MED1 has been the most extensively investigated among the Mediator subunits and
164 is recognized as a prominent transcriptional coactivator and a constituent of super-enhancers
165 (SEs)(Hnisz et al., 2013; Whyte et al., 2013). Intriguingly, silencing *Med1* resulted in a skewed
166 transcriptional profile towards repression which contrasts with the effect observed with *Med4*
167 silencing (Figure S2D; Table S6-S8). GSEA using metastatic and dormant signatures also
168 indicated that *Med1* reprograms the transcriptional profile in the opposite direction compared to
169 *Med4* (Figure S2E).
170
171 We then investigated the impact of *Med4* depletion on the 3D chromatin structure. ATAC-seq
172 analysis confirmed that *Med4* depletion led to a substantial increase in chromatin accessibility
173 (Figure 2B). Conversely, *Med1* silencing had minimal impact on chromatin accessibility (Figure
174 S2F). Complementary micrococcal nuclease (MNase) digestion assay(Mieczkowski et al., 2016)
175 aligned with the findings from ATAC-seq results, showing that *Med4* depletion led to
176 decompaction, particularly of poly-nucleosome part, indicative of heterochromatin structures
177 (Figure S2G). On the contrary, *Med1* silencing resulted in increased resistance to MNase,
178 suggesting that the downregulation of *Med1* caused chromatin structure to become more compact
179 (Figure S2H). To directly observe the impact of *Med4* depletion on 3D chromatin architecture, we
180 visualized chromatin using HP1α staining, a marker for constitutive heterochromatin(Wreggett et
181 al., 1994). Intriguingly, *Med4*-depleted cells displayed a sparse distribution of heterochromatin
182 foci accompanied by an increase in nuclear size, whereas the control cells exhibited a condensed
183 heterochromatin structure (Figure 2C, and Supplementary Movies 1-3). In contrast, *Med1*-depleted
184 cells did not exhibit significant changes in the distribution of heterochromatin foci (Figure S2I,
185 and Supplementary Movies 4-6), highlighting *Med4*'s distinct role in the spatial organization of
186 chromatin compared to *Med1*.

187 To delve deeper into the consequences of *Med4* silencing on chromatin structure and
188 transcriptional output, we integrated RNA-seq and ATAC-seq results. Upon depleting *Med4*, the
189 majority of genes exhibited significant changes in chromatin accessibility and gene expression,
190 with increased levels in both accessibility and transcription (Figure 2D). Gene ontology (GO)
191 analyses of genes showing concomitant changes in accessibility and gene expression (located in
192 the upper quadrant of the intersection between RNA-seq and ATAC-seq) indicated significant
193 enrichment of ECM-related and cell-adhesion-related gene signatures (Figure 2E). In particular,
194 the majority of differentially expressed genes (DEGs) after *Med4* silencing were collagen- (e.g.,
195 *Col1a1, Col1a2, Col6a1*), actomyosin-related (e.g., *Acta2, Myl9*), and ECM-remodeling genes
196 (e.g*., Loxl3, Mmp2, Adamts5*) (Figure 2F).

197 To confirm the link between chromatin structure and ECM gene expression regulated by *Med4*,
198 further profiling of genome-wide chromatin accessibility revealed that *Med4* downregulation alters
199 the promoter regions of DEGs, with upregulated DEGs exhibiting increased accessibility and
200 downregulated DEGs showing reduced promoter accessibility (Figure 2G and Figure S2J). This
201 suggests that *Med4* selectively modulates promoter chromatin accessibility, thereby influencing
202 gene expression in a context-dependent manner, particularly in the regulation of ECM genes
203 (Figure 2H).

204 Finally, this modulation of chromatin structure by *Med4* depletion is associated with stiffening
205 matrices surrounding cancer cells, so called desmoplasia, which is a critical manifestation of
206 cancer progression(Di Martino et al., 2022; Ishihara and Haga, 2022; Paszek et al., 2005; Ueno et
207 al., 2015). Immunohistochemistry (IHC) of α-SMA (a protein coded by *Acta2*) and Masson's
208 trichrome stain, which labels collagen, validated the substantial desmoplastic stromal reaction in
209 metastases induced by *Med4* silencing compared to the dormant niche (Figure 2I). Collectively,
210 these results indicate that *Med4* haploinsufficiency bolsters matrix stiffening, which creates a
211 favorable environment conducive to the metastatic outgrowth.

212 ***Med4* restrains enhancer priming and activation.**

213 We next explored how this chromatin structural change translates into broader epigenomic
214 reprogramming. Histone modifications, often found in recurring combinations at promoters,
215 enhancers, and repressed regions, serve as crucial markers for gene regulation (Barski et al., 2007;
216 Ernst and Kellis, 2010, 2012). We performed ChIP-sequencing for promoters (H3K4me3),
217 enhancers (H3K27Ac and H3K4me1), active transcription (H3K79me2), and heterochromatin
218 (H3K9me3). Notably, *Med4* depletion led to a marked increase in these histone modifications
219 particularly those associated with transcriptional activation (Figure S3A-S3E). To further dissect
220 the epigenomic reprogramming, we employed the ChromHMM algorithm to model combinatorial
221 patterns of the five histone modifications (Figure 3A). The resulting 10-state ChromHMM model
222 categorized various epigenomic states, including promoters (E03 and E04), distal enhancers (E05,
223 E06, and E07), genic or transcribed enhancers (E08 and E09), transcription (E10), and
224 heterochromatin (E02). *Med4* silencing led to an increase in active histone modifications in
225 promoter and enhancer regions, but slight decrease in heterochromatin regions (Figure S3F-S3I).
226 GO analyses of these chromatin states revealed that distal enhancer states were associated with
227 ECM gene signatures, consistent with our RNA-seq and ATAC-seq results (Figure 3B, and Figure
228 S3J). We thereby focused on distal enhancer states, which were subdivided by three categories:
229 active enhancers (E06), characterized by the enrichment of both H3K27Ac and H3K4me1; poised
230 (closed) or primed (open) enhancers (E07), marked by H3K4me1 alone, reflecting regions primed
231 for future activation; and weak enhancers (E05), marked by H3K27Ac alone. *Med4* depletion led
232 to an increase in both H3K4me1 and H3K27Ac deposition in active and poised enhancers with a
233 more robust increase in H3K4me1 (Figure 3C). Integration with ATAC-seq data revealed that
234 *Med4* depletion opens up poised enhancer regions, transitioning them to a more accessible, primed
235 state, ready for activation upon receiving the necessary cues (Figure 3D).

236 Enhancers are classified into super-enhancers (SEs) and typical enhancers (TEs). SEs, which are
237 clusters of enhancers with high levels of transcriptional co-activators, are crucial for regulating
238 key genes involved in cell identity and disease(Hnisz et al., 2013; Whyte et al., 2013). To explore
239 the epigenomic reprogramming induced by *Med4* depletion, we extended our analysis to include

240 the identification and characterization of SEs. Our analysis showed that *Med4* depletion increases
241 the intensities of both H3K4me1 and H3K27Ac at their respective SE and TE regions (Figure S4A-
242 S4D). Interestingly, *Med4* silencing led to a significant increase in the number of H3K4me1-
243 enriched SEs (455 in NTC versus 1,296 in shMed4) and TEs (18,139 in NTC versus 26,040 in
244 shMed4) compared to the H3K27Ac-enriched SEs (683 in NTC versus 630 in shMed4) and TEs
245 (15,292 in NTC versus 16,132 in shMed4) (Figure 3E and 3F). The intersection of SEs between
246 NTC and *Med4*-silenced cells reveals a substantial increase in *de novo* H3K4me1-enriched SEs
247 (Figure 3G), which are associated with cell-cell adhesion, focal adhesion, and collagen-related
248 ECM (Figure S4E and S4F). While the number of *de novo* H3K27Ac-enriched SEs did not
249 significantly change compared to H3K4me1-enriched SEs, the intensity of H3K27Ac marks
250 increased significantly in *Med4*-depleted cells, suggesting that *Med4* depletion contributes to the
251 full activation of SEs. The *Col6a3* gene exhibits both a *de novo* H3K4me1-enriched SE and a
252 persistent SE, each with significantly higher H3K4me1and H3K27Ac intensities compared to the
253 control (Figure 3H). Collectively, these observations suggest that *Med4* inhibits H3K4me1
254 deposition, preventing the transition of enhancers from a poised to an active state. This inhibition
255 restricts epigenomic reprogramming and ECM gene expression.

256 ***Med4* suppresses cancer stemness and expansion in a desmoplastic niche.**

257 Given the functional similarities between metastasis-initiating cells and cancer stem cells (CSCs)
258 (Malanchi et al., 2011), we hypothesized that *Med4* might regulate CSC traits. Indeed, GSEA
259 showed enrichment of the Wnt pathway in *Med4*-depleted cells, a pathway known to be associated
260 with cancer stemness (Figure S5A) (Reya and Clevers, 2005). *Med4*-depleted cells exhibited a
261 substantial increase in their self-renewal capacities, demonstrated by the increased number and
262 size of tumor spheres (Figure S5B and S6A), enhanced clonogenicity (Figure S5C and S6B), and
263 improved anchorage-independent growth (Figure S5D and S6C). In addition, *Med4*-depleted cells
264 exhibited increased migratory (Figure S5E and S6D) and invasive (Figure S5F) capacities which
265 are common characteristics of cells undergoing epithelial to mesenchymal transition
266 (EMT)(Pastushenko and Blanpain, 2019). Overall, these results suggest that *Med4* depletion
267 endows dormant cancer cells with self-renewal capacities.

268 As CSCs exhibit preferential growth in a stiff matrix, a hallmark of the tumor microenvironment,
269 this suggests that mechanical cues from the ECM can synergize with intrinsic stemness to promote
270 cancer cell metastatic abilities (Li et al., 2023; Liu et al., 2023). Thus, we sought to examine if
271 *Med4* mediates outgrowth in response to the stiffness and composition of matrices. To model a
272 normal ductal microenvironment characterized by a basement membrane-rich ECM, and a stiff
273 tumor microenvironment enriched in collagen I(Egeblad et al., 2010; Paszek et al., 2005), we
274 placed control and *Med4*-silenced breast cancer cells in two different conditions: (1) 3D Matrigel,
275 representing the basement membrane-rich ECM, and (2) 3D Matrigel plus collagen I, which
276 recapitulates the tumor microenvironment. Strikingly, *Med4* depletion promoted tumor organoid
277 growth and invasion in stiff 3D matrices (Matrigel + collagen I), while cells maintained a spherical
278 growth pattern in the soft 3D matrices (Matrigel-only) regardless of their *Med4* expression (Figure
279 4A). These data indicate that cells with a *Med4*-haploinsufficient background can preferentially
280 grow in the desmoplastic niche. Collectively, these results indicate that *Med4* haploinsufficiency
281 not only induces matrix stiffening, but also stimulates the cancer-cell intrinsic survival and
282 proliferative abilities within the established metastatic niche.

283 ***Med4* suppresses integrin-mediated nuclear mechanosensing.**

284 To exit dormancy, metastatic cancer cells extend lamellipodia and establish productive interactions
285 with the matrix. Adhesion molecules, particularly integrins, play a crucial role in transmitting
286 external stimuli from the ECM(Barkan et al., 2010; Case and Waterman, 2015; Kechagia et al.,
287 2019). Considering the transcriptional alterations in the ECM composition (Figure 2E) and integrin
288 repertoire (Figure S7A) by *Med4* depletion, we hypothesized that *Med4* haploinsufficiency
289 promotes metastatic reactivation by activating integrin-mediated signaling. Immunofluorescence
290 analysis revealed that *Med4*-silenced cells exhibit a more organized actin cytoskeleton and more
291 numerous focal adhesion plaques (Figure 4B and S7B). Our data also show that phosphorylation
292 of key integrin signaling molecules was significantly increased upon *Med4* depletion (Figure S7C).
293 Collectively, these findings provide evidence that *Med4* inhibits integrin signaling activation.

294 To identify the top transcription factors controlling the transcriptome changes by *Med4* silencing,
295 we applied ChIP-X Enrichment Analysis 3 (ChEA3) transcription factor enrichment analysis to
296 the RNA-seq data(Keenan et al., 2019). Notably, we found that SRF, and TEAD 1/2 cistromes
297 govern the transcriptional reprogram by *Med4* depletion along with EMT cistromes (Figure 4C).
298 Also, *de novo* motif enrichment analysis performed on genes exhibiting concurrent increases in
299 accessibility and gene expression following *Med4* silencing confirmed the enrichment of TEAD,
300 TEAD4, and SRF motifs (Figure S8A). SRF, a co-factor for myocardin-related transcription factor
301 (MRTF), and TEADs, transcriptional co-activators for YAP and TAZ, are major mechanosensitive
302 transcriptional factors that transduce mechanical cues by the cytoskeleton to gene expression in
303 response to integrin-mediated adhesion. GSEA results revealed that the gene signatures for
304 MRTF/SRF(Esnault et al., 2014) and for YAP(Cordenonsi et al., 2011) are enriched in *Med4*-
305 depleted cells (Figure 4D). In response to both biochemical and mechanical signals, YAP
306 undergoes translocation from the cytoplasm to the nucleus, where it interacts with and triggers the
307 activation of the TEAD transcription factor(Zhao et al., 2008). MRTF binds stoichiometrically to
308 soluble G-actin and is released as a consequence of actin polymerization and formation of stress
309 fibers. Once released from G-actin, MRTF enters into the nucleus, where it functions as a co-factor
310 for SRF, which drives expression of cytoskeletal genes in a feed forward loop(Posern and
311 Treisman, 2006). Hence, we sought to investigate whether mechanosensitive transcription factors,
312 specifically MRTF and YAP, were activated upon *Med4* depletion. We observed activation of
313 MRTF/SRF target genes(Calvo et al., 2013; Foster et al., 2017), YAP/TEAD target genes(Dupont
314 et al., 2011), and shared MRTF and YAP target genes in *Med4*-depleted cells (Figure 4E).
315 Immunofluorescence results revealed that *Med4* silencing leads to nuclear localization of both
316 MRTF-A and YAP (Figure 4F). To address the discrepancy between MRTF and YAP activation,
317 we conducted time-course experiments using a doxycycline-inducible promoter for *Med4* shRNAs
318 (Figure S8B-S8F). Our findings demonstrated that mRNA levels of MRTF/SRF target genes were
319 significantly upregulated at 24 hours post-, whereas activation of the YAP/TEAD pathway was
320 less robust and occurred 3 to 5 days later, prompting us to conclude that *Med4* depletion activates
321 MRTF to a greater degree than YAP. Restoring MED4 expression by overexpressing *MED4*
322 cDNA led to the relocation of MRTF-A to the cytoplasm and resulted in the reversal of MRTF-
323 A/SRF target gene expression (Figure S8G and S8H). To determine if these integrin-mediated
324 mechanosensitive transcription factors play a pivotal role for *in vivo* metastatic reactivation by
325 *Med4* depletion, we depleted these mechanosensitive transcription factors though shRNA
326 silencing and injected cancer cells into immunocompetent BALB/c recipients (Figure S8I).
327 Silencing *Mrtfa*, *Srf,* or *Yap* + *Taz* abrogated the metastatic capacity of *Med4*-silenced cells,

328 pointing to a requirement for these transcriptional regulators in driving metastatic reactivation
329 (Figure 4G). Together, these findings indicate that *Med4* restrains the initiation of integrin-
330 mediated mechanotransduction to maintain dormant states.

331 ***MED4* haploinsufficiency correlates with poorer prognosis in breast cancer.**

332 To explore the clinical relevance of *MED4* status in breast cancer patients, we examined *MED4*
333 expression and prognosis in multiple metastatic breast cancer datasets from cBioportal(Cerami et
334 al., 2012; Gao et al., 2013). *MED4* exhibited shallow deletions in almost 40% of human breast
335 cancer metastasis samples (Figure 5A, Figure S9A and S9B)(Lefebvre et al., 2016). The low
336 proportion of deep deletions further underscores *MED4* as an essential gene. Consistent with
337 genomic analysis, paired RNA-seq revealed that mRNA levels of *MED4* are lower but not
338 undetectable in lung, liver, and brain metastases than in matched primary tumors (Figure
339 5B)(Siegel et al., 2018). Intriguingly, Kaplan-Meier analysis of primary tumor datasets revealed
340 that *MED4* expression levels could be used to stratify patients into high- and low-risk groups in
341 terms of recurrence-free survival; lower *MED4* levels in primary tumors were strongly correlated
342 with poor prognosis in patients with advanced breast cancer across subtypes (Figure 5C and Figure
343 S9C)(Gyorffy et al., 2010). Furthermore, lower levels of *MED4* mRNA can serve as a prognostic
344 indicator for poor overall survival, particularly in subgroups of patients with estrogen receptor-
345 negative (ER-) or human epidermal growth factor 2-positive (HER2+) breast cancer (Figure S9D
346 and S9E). We confirmed the prognostic value of *MED4* gene via SurvExpress platform. *MED4*
347 could effectively stratify patients into high and low-risk groups for distant metastasis-free survival
348 (DMFS), with lower *MED4* expression in high-risk group (Figure 5D). Finally, the *MED4*-
349 associated ECM gene signature (Figure 2F) was found to be associated with DMFS, further
350 validating its predictive capability (Figure 5E). Collectively, these results suggest that *MED4* and
351 its associated gene signatures could be prognostic markers to predict metastatic relapse in breast
352 cancer.

353 **Discussion**

354 In this study, a genome-scale screen and functional *in vivo* assays identified and validated *Med4*
355 as a critical gatekeeper of breast cancer metastasis dormancy. Mechanistically, we establish that
356 *Med4* depletion causes decompaction of 3D chromatin structure and initiates a novel enhancer
357 reprogramming event, wherein H3K4me1 deposition transforms weak and poised enhancers into
358 more active states. This enhancer reprogramming unlocks ECM gene expression, activates
359 integrin-mediated mechano-transduction, and facilitates the emergence of cancer cells from
360 dormancy in metastatic niches. Correspondingly, clinico-genomic analyses reveal that
361 heterozygosity and associated lower expression of *MED4* correlates with worse prognosis and
362 decreased metastasis-free survival. Thus, this work highlights a previously unrecognized role of
363 *Med4* haploinsufficiency in regulating enhancers and gene expression programs that promote
364 functional tropism and metastatic reactivation (Figure 5F).

365 We demonstrate that *Med4* haploinsufficiency has the potential to initiate metastatic reactivation
366 within the context of breast cancer. Interestingly, our analysis reveals that *Med4* silencing
367 predominantly stimulates a transcriptional profile consisting of ECM-related genes, which stands
368 in contrast to the Mediator's conventional role in transcription. Conversely, the silencing of *Med1*
369 displayed a unique and directionally oppositional function that MED4 serves within the context of

370 Mediator-mediated transcription, highlighting the considerable flexibility of the complex
371 contingent on its subunit composition. Sun and colleagues conducted a shRNA screening targeting
372 individual subunits of transcription factor IID (TFIID) and the Mediator complex(Sun et al., 2021).
373 Disrupting various subunits yielded distinct effects on the transcriptome of mouse embryonic stem
374 cells (mESCs), even within subunits of the same complex. Their shRNA-based screen, similar to
375 our findings, revealed that *Med4* shRNA altered transcriptome towards activation, and gene
376 ontology analysis of the up-regulated gene list highlighted the enrichment of ECM signatures.
377 However, when they employed the auxin degron system for the acute degradation of MED4, it had
378 a minimal effect on the integrity of the Mediator complex and resulted in transcriptome
379 downregulation by decreasing RNA polymerase II recruitment to the promoters. Hence, it is
380 plausible that a dosage effect whereby *Med4* knockdown as opposed to complete knockout drives
381 the pathological phenotype.

382 The Mediator complex regulates transcription by linking enhancers to promoters, with super-
383 enhancers characterized by high Mediator binding and associated with key genes and
384 oncogenes(Whyte et al., 2013). While the term 'Mediator' is often used as a general marker for
385 defining SEs, it is commonly represented by only MED1 and MED12(Guo et al., 2019; Hnisz et
386 al., 2013). To address the controversial role of *Med4* in transcriptional repression, we focused on
387 its impact on epigenomic reprogramming. Our integrated analysis of RNA-seq, ATAC-seq, and
388 histone ChIP-seq data reveals that *Med4* depletion leads to significant epigenomic reprogramming,
389 making the genome more permissive to transcriptional activation. We found that distal enhancers
390 marked by H3K4me1 and H3K27Ac play a crucial role in differential gene expression, consistent
391 with the established role of super-enhancers in defining cell identity. Specifically, *Med4*
392 knockdown leads to a notable increase in H3K4me1 deposition at the enhancer regions compared
393 to H3K27Ac, and differential expression and chromatin accessibility were correlated with distal
394 enhancer reprogramming. This suggests that *Med4* plays a significant role in keeping enhancers in
395 a poised state, and its depletion shifts the balance toward preparing more enhancers for potential
396 activation, thus contributing to epigenomic reprogramming and altered gene expression,
397 particularly in ECM genes. Our results revealed that *Med4* selectively regulates chromatin
398 accessibility at promoter regions of differentially expressed genes. Recent studies indicate that
399 H3K4me1 facilitates enhancer-promoter interactions(Kubo et al., 2024), suggesting that *Med4*
400 depletion may facilitate the interaction between activated and primed enhancers with opened
401 promoter region. Further investigation using Hi-C or promoter capture Hi-C is needed to explore
402 these enhancer-promoter interactions in detail. Additionally, biochemical studies are required to
403 elucidate how *Med4* directly regulates H3K4 monomethylation, potentially involving H3K4
404 mono-methyltransferases such as KMT2C or KMT2D(Alam et al., 2020). Moreover, it is worth
405 noting that *Med4* depletion led to a significant increase in nuclear size, which may contribute to
406 the observed spatial reconfiguration in 3D chromatin structure. Given that the nuclear lamina is
407 known to anchor heterochromatin to the nuclear periphery for gene silencing (Reddy et al., 2008;
408 van Steensel and Belmont, 2017), future investigations into the impact of nuclear architecture
409 changes could provide deeper insights into the mechanisms governing chromatin organization.

410 Current adjuvant treatment for breast cancer is aimed to prevention of metastatic relapse, and
411 despite the prognostic value of pathological, genomic, and transcriptional testing, late metastasis
412 occurs in nearly 25% of patients(Berry et al., 2005). Elucidating the molecular mechanisms that
413 enable dormant tumor cells to evade the immune system and survive at early metastatic sites, as
414 well as identifying subsets of patients who could benefit from therapy targeting these mechanisms

415 may reduce the mortality related to metastatic relapse. We found that a large fraction of metastatic
416 breast cancer samples from patients have shallow *MED4* deletions (Figure 5A, S9A and S9B), and
417 lower *MED4* levels correlated with poor prognosis in patients with advanced breast cancer across
418 subtypes (Figure 5C-5D and S9C-S9E), suggesting that *MED4* may play a critical role in
419 governing metastatic dormancy in breast cancer patients.
420
421 Our findings highlight the potential of *MED4* expression and related gene signatures as a
422 biomarker of metastatic dormancy. Future studies will investigate whether *MED4* can stratify
423 patients prone to recurrence, enabling the identification of subsets at high risk for subclinical
424 metastasis and may uniquely benefit from therapeutic intensification. Moreover, these data lay the
425 foundational groundwork for novel strategies targeting effectors activated by *MED4*
426 haploinsufficiency including inhibitors of the FAK or YAP/TEAD pathways.

427 **Materials and Methods:**
428
429 **Animal studies**

430 Mouse studies were conducted in accordance with protocols approved by the Institutional Animal
431 Care and Use Committee of Columbia University and MD Anderson Cancer Center. Six-week-old
432 female mice BALB/c were purchased from The Jackson Laboratory.
433 To examine lung colonization, 4T07 (3.0 x 10^5), D2A1-d (2.0 x 10^5), and D2A1 (2.0 x 10^5)
434 mammary carcinoma cells were resuspended in 100 µl of PBS and injected into the lateral tail vein.
435 Doxycycline (Dox) was administered to mice through water *ad libitum* (2 mg/ml). For inducible
436 shRNA experiments, Dox was administered either immediately after injection (Dox day 0) of the
437 cancer cells or 14 days later (Dox day 14). Bioluminescence (BLI) was used to examine metastatic
438 outgrowth. Metastatic lesions were confirmed by postmortem dissection. To examine multi-organ
439 colonization, D2A1-d-TGL (8.0×10^4) cells were injected into the left ventricle of BALB/c mice
440 in 100 µl of PBS.
441 For bioluminescent imaging, mice were anesthetized and injected retro-orbitally with 1.5 mg (75
442 mg/kg) of D-luciferin (Gold Biotechnology; LUCK-1G) at the indicated times after injecting cells.
443 Animals were imaged in an IVIS Spectrum chamber within 5 min after D-luciferin injection, and
444 data were recorded using Living Image software (PerkinElmer). To measure lung colonization,
445 photon flux was calculated for each mouse by using a circular region of interest encompassing the
446 thorax of the mouse. After subtracting a background value obtained from a control mouse injected
447 only with D-luciferin, photon flux was normalized to the value obtained 30 min after injection of
448 the tumor cells. This latter value was arbitrarily set at 100. For *ex vivo* analysis, anesthetized mice
449 were injected with D-luciferin. Mice were euthanized 15 min later, and organs were rapidly
450 dissected for analysis.

451 **Cell lines**

452 The 4T07 cell line was generously provided by Dr. Fred Miller (Wayne State University, Detroit,
453 MI) and cultured as described (Aslakson and Miller, 1992). The D2A1-d and D2A1 cell lines were
454 generously provided by Dr. Robert Weinberg (MIT, Boston, MA) and cultured as described(De
455 Cock et al., 2016). HEK293FT cells (from Thermo Fisher Scientific) was cultured per the
456 manufacturer's protocol. For bioluminescent tracking, cell lines were infected with a lentiviral
457 vector encoding herpes simplex 3 virus thymidine kinase 1, green fluorescent protein (GFP) and
458 firefly luciferase. The top 10% of GFP-positive cells were isolated by FACS to ensure uniform
459 expression levels of GFP across all cell populations, mitigating any potential artificial effects
460 caused by GFP's immunogenicity.

461 **Generation of stable cell lines by lentiviral transduction**

462 Stable cells were generated by lentiviral transduction as described in with a minor modification.
463 In the case of constitutively expressing stable cells, all experiments were conducted within a 1 to
464 3-week window from transduction to minimize the counterselection effect of *Med4* depletion
465 unless otherwise specified. In the case of cells expressing doxycycline-inducible constructs, the
466 indicated time frame starts from the initiation of doxycycline treatment.

467 **Genome-wide CRISPR-Cas9 screening.**

468 A forward genetic screening was performed as described in with a minor modification(Gao et al.,
469 2014). The GeCKO v2 library A was obtained from Addgene (1000000052) and was amplified
470 and packaged in lentiviruses as described previously(Joung et al., 2017). The viral titer was
471 determined by limiting dilution-colony counting. 4T07 cells were transduced with the library at
472 the MOI of 0.3 to ensure one sgRNA/cell. Library-transduced cells were selected with 2 μg/ml of
473 puromycin for 7 days, and then injected through tail vein of 6-week-old female BALB/c mice.
474 Mice were monitored weekly by bioluminescent imaging and lung metastases were confirmed by
475 postmortem dissection at 3-4 weeks after injecting library-transduced cells. Macroscopic lung
476 nodules were dissected separately and digested in Collagenase Type IV (Stem Cell technologies;
477 07909) at 37°C for 1.5 h with rocking. After centrifuging at 1,000 rpm for 3 min, pellets were
478 resuspended in the complete medium and filtered through 35 μm strainers. Isolated clonogenic
479 tumor cells were expanded in 4 μg/ml of puromycin medium. Genomic DNAs were isolated using
480 Maxwell® RSC Cultured Cells DNA Kit (Promega; AS1620) according to the manufacturer's
481 protocol. Inserted sgRNA sequences were amplified by PCR with the following primers and
482 thermocycling parameters (v2Adaptor-F: 5'-
483 AATGGACTATCATATGCTTACCGTAACTTGAAAGTATTTCG-3', v2Adaptor-R: 5'-
484 TCTACTATTCTTTCCCCTGCACTGTTGTGGGCGATGTGCGCTCTG-3'; 95°C for 2 min, 30
485 cycles of (98°C for 1 s, 60°C for 5 s, 72°C for 35 s), and 72°C for 1 min)
486 All PCR was performed using KAPA HiFi HotStart ReadyMix (Kapa Biosystems; KK2602). The
487 PCR products were isolated by QIAquick PCR Purification Kit (Qiagen; 28104) and subjected to
488 Sanger sequencing to discern single entities that can reactivate metastasis. Consequently, we
489 identified 26 metastases, each associated with a single sgRNA, which were discernible through
490 Sanger sequencing. The table listing the gene names and corresponding sgRNA sequences is
491 provided in **Table S1**. To validate hits, the sgRNAs were cloned in lentiCRISPR v2 vector, and
492 transduced into 4T07-TGL cells. Transduced clones were injected through tail vein of 6-week-old
493 female BALB/c mice and lung metastases were monitored weekly by bioluminescent imaging to
494 prioritize hits.

495 **Indel analysis for validating a knockout screening.**

496 A pair of primers was designed to amplify the 250-300 bp region centered around the sgRNA cut
497 site (GRCm39 chr.14 73752726-73752745). 300 ng of genomic DNA isolated in *Genome-wide*
498 *CRISPR-Cas9 screening* was amplified by PCR with the following primers and thermocycling
499 parameters (*Med4* indel primer_F: 5'-CACGGCCATGGCTTTCTAAC-3', *Med4* indel primer_R:
500 5'- GAGGGTTGTGAGCTACGTGT-3'; 95°C for 2 min, 30 cycles of (98°C for 1 s, 60°C for 5 s,
501 72°C for 35 s), and 72°C for 1 min). PCR was performed using NEBNext® High-Fidelity 2X PCR
502 Master Mix (NEB; M0541S). The purified PCR products were separated by a 4-20% TBE gel
503 (Invitrogen; EC62252BOX) and stained with GelRed for 1 hr. The bands were visualized by
504 ChemiDoc (Bio-Rad).
505

506 **DNA constructs for overexpression and silencing.**

507 The cDNA encoding human *MED4* was obtained from Addgene (15425). The cDNA was sub-
508 cloned in FLAG-HA-pcDNA3.1- (Addgene; 52535) to generate N-terminally Flag-HA tagged
509 MED4 cDNA. The N-term Flag-HA-MED4 cDNA was sub-cloned in pCDH-EF1-MCS-IRES-
510 Neo (System Biosciences; CD502A-1) and verified by sequencing. The shRNAs were designed
511 using the SplashRNA algorithm(Pelossof et al., 2017). shRNA sequences are shown in **Table S9**.

512 **Cell growth assay**

513 Cells were seeded at a density of 1.0 x 10^5 cells onto 6 cm dishes (D2A1-d cells) or 10 cm dishes
514 (4T07 cells) at Day 0. Cells were trypsinized and counted at the indicated.
515
516 **Tumorsphere assay**

517 Single cells suspension of 4T07, D2A1-d, and D2A1 cells (10,000 cells/ 2 ml) were plated on 6-
518 well ultra-low attachment plates for tumorsphere cultures. Cells were cultured in serum free
519 MEBM supplemented with 1:50 B27, 10 ng/ml bFGF (BD Biosciences;) and 20 ng/ml EGF (BD
520 Biosciences;) and 4 ug/ml insulin, 4 ug/ml heparin, and 0.4% BSA for 10 days. Tumorsphere were
521 visualized under phase contrast microscope, photographed and counted by GelCounter and
522 represented graphically.
523
524 **Soft agar colony formation assay**

525 6-well culture plates were coated with 1 ml of 0.6 % Low Melt Agarose (Bio-Rad; 1613111). Cells
526 were diluted at a density of 1.0 x 10^4 cells/ml in media containing 0.3% Low Melt Agarose and
527 seeded 1 ml/ well. After 10 days, cells were stained with 0.005% crystal violet in 10% neutral
528 buffered formalin (NBF) for 30 min at R.T. Soft agar was destained with distilled water until the
529 background got clear. Colonies were scanned for visualization and counted manually.
530
531 **3D culture**

532 8-well chamber slides were coated with either 100 µl of 100% Matrigel (Corning; 354263) or 50%
533 Matrigel + 50% Collagen I (Corning; 354236) at 37°C for 30 min prior to cell seeding (Nguyen-
534 Ngoc et al., 2015). Cells were seeded onto the matrix at a density of 400 cells/100 µl/well.
535
536 **Clonogenicity assay**

537 For measuring clonogenicity capacities, D2A1-d and 4T07 cells were seeded onto 10 cm dishes at
538 a density of 1,000 cells. After 6 days, the morphology and size of colonies were captured by a
539 phase-contrast microscopy. Cells were fixed with 100% methanol for 20 min and stained with 0.5%
540 crystal violet in 20% methanol for 5 min. Then plates were destained with PBS until the
541 background got clear. The images of whole plates were taken by a scanner and colonies were
542 counted manually.
543
544 **Transwell migration/invasion assay**

545 Migration assays were performed as previously described in (Bae et al., 2015) with minor
546 modification. using uncoated cell culture inserts with 8 µm pores (Corning; 3422) according to
547 manufacturer's instructions. Briefly, D2A1-d and 4T07 cells were harvested with Trypsin/EDTA
548 and resuspended in serum-free medium at a density of 1.0 x 10^5 cells/ml for D2A1-d and 2.0 x 10^5
549 cells/ml for 4T07. 100 µl of cells were seeded into the upper chamber of uncoated cell culture
550 inserts with 8 µm pores (Corning; 3422). Lower chambers were filled with 650 µl medium
551 containing 10% FBS as a chemoattractant. After 18 hours, cells were fixed and permeabilized with
552 70% ethanol for 15 min and stained with 0.1% crystal violet/10% ethanol for 20 min. The non-

553 migrating cells on the upper surface of the filter were removed by cotton swab. The number of
554 migratory cells was measured by counting at × 200 magnifications using a microscope. For
555 invasion assays, Matrigel was diluted in ice-cold serum-free medium to a concentration of 300
556 µg/ml. 100 µl of diluted Matrigel solution was added into the upper chamber and incubated at
557 37°C for 30 min to coat the membrane. D2A1-d (1.0 x 10^4 cells) and 4T07 (3.0 x 10^4 cells) cells
558 were seeded into the upper chamber and incubated for 24 hours. The following procedure was
559 performed as described above.
560

561 **Micrococcal nuclease digestion assay (MNase digestion assay)**

562 Global chromatin accessibility was assessed by MNase digestion assay as described
563 previously(Cheng et al., 2019) with minor modification. 1 million cells were cross-linked with 1%
564 formaldehyde for 10 min at R. T. and quenched with 125 mM glycine for 5 min. Cells were washed
565 once with cold PBS and collected by centrifuging at 1,000 rpm for 5 min at 4°C. Fixed cells were
566 re-suspended in lysis buffer (10 mM Tris-HCl, pH7.5, 10 mM NaCl, 0.5% NP-40) and incubated
567 on ice for 10 min. After centrifugation, the cell pellets ware washed once with MNase digestion
568 buffer (20 mM Tris-HCl, pH7.5, 15 mM NaCl, 60 mM KCl, 1 mM $CaCl_2$). After re-suspended in
569 250 µl MNase digestion buffer with proteinase inhibitors, 62.5 units per 1 million cells MNase
570 (NEB; M0247S) was added to resuspended pellets. After incubation at 37°C for the indicated time,
571 250 µl of STOP buffer (100 mM Tris-HCl, pH 8.1, 20 mM EDTA, 200 mM NaCl, 2% Triton X-
572 100, 0.2% sodium deoxycholate) was added. Lysates were sonicated for 4 cycles (30 sec on and
573 30 sec off) in Bioruptor and supernatant was collected after centrifugation. The supernatant was
574 reverse-crosslinked at 65°C overnight and treated with RNase A at 37°C for 1 h and Proteinase K
575 at 55°C for 2 h. The DNA fragments were purified by ethanol precipitation and analyzed by
576 agarose gel electrophoresis.

577 **Immunofluorescence**

578 For staining cells on 2D culture, cells were rinsed with PBS once and fixed with 4%
579 paraformaldehyde (PFA) in PBS for 15 min. Cells were washed three times with PBS for 5 min
580 followed by permeabilizing with 0.5% Triton X-100/PBS for 5 min. After rinsing once with PBS,
581 cells were blocked with 1% BSA/0.3% Triton X-100/PBS for 1 h. Next, cells were incubated in
582 primary antibodies diluted in the blocking buffer at 4°C overnight followed by incubating in the
583 secondary antibodies for 1 h R.T. After washing once with PBS, nuclei were counter-stained with
584 DAPI (1:1000 in PBS) for 5 min followed by mounting.
585 For staining cells on 3D culture, cells were fixed with 2% PFA in PBS supplemented with 50 mM
586 glycine for 30 min at R.T. After washing three times for 20 min with PBS supplemented with 50
587 mM glycine, cells were blocked with 10% normal goat serum in the IF buffer (0.1% BSA, 0.2%
588 Triton X-100, 0.05% Tween-20 in PBS) at R.T. for 1 h. Primary antibodies were diluted in the
589 blocking buffer and subjected to cells. After overnight incubation at 4°C, cells were washed with
590 the IF buffer for 20 min three times and followed by incubating with secondary antibodies (diluted
591 in the blocking buffer) for 1 h at R.T. After washing once with the IF buffer, nuclei were counter
592 stained with DAPI for 5 min, followed by mounting.

593 **Immunohistochemistry**

Immunostaining of mouse lungs was performed as previously described.(Gao et al., 2016) In brief, tissues were fixed in 10% neutral buffered formalin for 24 hours, embedded in paraffin, sectioned, and stained with hematoxylin and eosin (H&E) for histopathological evaluation. For immunohistochemistry, unstained slides of sectioned tissues were deparaffinized and epitope/antigen retrieval was performed with 10 mM sodium citrate (pH 6.0). The slides were treated with 3% H2O2 to block endogenous peroxidase. The slides were then incubated in 5% normal goat serum/5% BSA/0.3% Triton X-100/PBS and stained with the appropriate primary antibodies. After an overnight incubation in primary antibodies, slides were stained with secondary antibodies and hematoxylin before mounting with the Vectashield mounting medium (Vector Laboratories).

Western blot

Protein lysates were harvested with RIPA lysis buffer (Sigma Aldrich; R0278) containing protease inhibitor cocktail (Thermo Fisher Scientific; 78429), phosphatase inhibitor 2 and 3 (Sigma Aldrich; P5726and P0044). Samples were standardized for protein concentration using the Pierce BCA protein assay (VWR 23227), and incubated at 100 °C for 10 min under reducing conditions. After denaturation, samples were separated by Bolt 4–12% Bis-Tris Plus Gels (Thermo Fisher Scientific NW04125BOX) and transferred onto a PVDF membrane using iBlot Transfer Stacks (Thermo Fisher Scientific IB401001). Blots were blocked with 5% bovine serum albumin (BSA) in TBST for 1 h at room temperature. Blots were then probed with different primary antibodies (listed in **Table S10**) in the blocking buffer overnight at 4 °C. Blots were washed with TBST for 10 min three times before incubation with secondary antibodies [Anti-rabbit IgG-HRP (Cell Signaling Technology 7074S, 1:5000), Anti-mouse IgG-HRP (Cell Signaling Technology 7076S, 1:5000), anti-goat IgG-HRP (Santa Cruz Biotechnology sc-2354, 1:5000)] in 2.5% BLOT-QuickBlocker (G Biosciences 786-011) in TBST for 1 h at room temperature. Blots were washed with TBST and imaged using chemiluminescent substrate [Pierce ECL (Thermo Fisher Scientific 32209), SuperSignal West Pico PLUS (Thermo Fisher Scientific 34577), or SuperSignal West Femto (Thermo Fisher Scientific 34096)] on the ChemiDox XRS + (Bio-Rad).

Real time PCR analysis

Total RNA was extracted using the Maxwell® RSC simplyRNA Cells and RNase-free DNase Kit (Promega; AS1390) using an automated RNA/DNA isolation instrument (Maxwell, Promega). cDNAs were synthesized using High-Capacity cDNA Reverse Transcription Kit (Applied Biosystems; 4368814). cDNA corresponding to approximately 10 ng of starting RNA was used for one reaction. qRT-PCR was performed with PowerUp SYBR Green Master Mix (Applied Biosystems) on QuantStudio™ 7 Flex Real-Time PCR System. All quantifications were normalized to endogenous GAPDH. Primer sequences used to amplify genes were purchased from Sigma-Aldrich and are listed in **Table S11**.

Bulk RNA-sequencing and analysis

Total RNA was isolated as described above. RNA-sequencing was performed by the BGI sequencing facility in Hong Kong. RNA quality, including RNA concentration, RIN value, 28S/18S ratio, and fragment length distribution was confirmed with an Agilent 2100 Bio analyzer (Agilent RNA 6000 Nano Kit). Libraries were prepared by using the standard methodology and

run on a BGISEQ-500 platform. Raw reads were quality-checked and subsequently mapped to the mouse genome (mm10_UCSC) through the Spliced Transcripts Alignment to a Reference (STAR)(Dobin et al., 2013), which outputs a BAM file containing both the sequence and its genomic coordinate. Together with a General Transfer Format (GTF) the file containing all the genomic annotations were used to determine the total number of reads per transcript using the HTSeq Count program.(Anders et al., 2015) Differential gene expression was analyzed by using the DESeq2 algorithm(Love et al., 2014) with |fold change| $\geq$ 2 and FDR < 0.05. Gene set enrichment analysis (GSEA) was performed on a pre-ranked gene list that was generated based on the gene expression changes between sh*Med4* and control cells(Subramanian et al., 2005). Gene expression data were transformed in logarithmic scale and normalized accordingly. Heatmaps showing the gene expression differences between control and *Med4* KD cells were generated by using the Morpheus online tool (https://software.broadinstitute.org/morpheus/).

ATAC-sequencing and analysis

Chromatin accessibility assays utilizing the bacterial Tn5 transposase were performed as described with minor modifications (Buenrostro et al., 2013). Cells (5.0×10^4) were lysed and incubated with transposition reaction mix for 30 minutes at 37°C. Samples were PCR-amplified and sequenced on an Illumina NextSeq 500. Bulk ATAC-seq raw data were pre-processed using the nfcore/atacseq pipeline version 2.0 (10.5281/zenodo.2634132), implemented in Nextflow (version 22.10.2). Reads were trimmed for both quality and Illumina adapter sequences using 'trim_galore' then aligned to mouse assembly mm39 with BWA using the default parameters. Aligned reads with the same start site and orientation were removed using the Picard tool MarkDuplicates (http://broadinstitute.github.io/picard). Density profiles were created by extending each read to the average library fragment size and then computing density using the BEDTools suite (http://bedtools.readthedocs.io). Reads were not extended when generating ATAC-seq read density. Enriched regions were discovered using MACS2 and scored against matched input libraries (|fold change| > 2 and p-value < 0.005). Peaks were then filtered against genomic 'blacklisted' regions and filtered peaks within 500 bp were merged to create a full peak atlas. Raw read counts were tabulated over this peak atlas using featureCounts (http://subread.sourceforge.net). All genome browser tracks and read density tables were normalized to a sequencing depth of ten million mapped reads. Peaks were annotated using linear genomic distance, with a gene assigned to a peak if it was within 50 kb upstream or downstream of the gene start or end, respectively. Motif signatures were obtained using the 'de novo' approach in Homer v4.7.2 (http://homer.ucsd.edu). The 'DESeq2' package in R was employed to identify differential gene expressions and accessibility with the threshold of absolute $\log_2$ FoldChange > $\log_2$ (1.5) and FDR $\leq$ 0.1. When a single gene was linked to multiple ATAC-seq peaks, all associated peaks were retained for analysis. A contingency plot was used to visualize the integrated results from ATAC-Seq and RNA-Seq data. Each quadrant in the plot indicates the statistical significance of either high or low expression for gene expression or accessibility.

ChIP-seq Analysis

Chromatin immunoprecipitation was performed as described (Terranova et al., 2018) with optimized shearing conditions and minor modifications. The antibodies used were: H3K4me1 (Abcam ab8895), H3K27ac (Abcam ab4729), H3K4me3 (Abcam ab8580), H3K9me3 (Abcam ab3594), H3K27me3 (Abcam ab8898). Sequencing reads were aligned to the mouse reference

genome (mm39) using BWA-MEM. SAM files were then converted to BAM format, sorted, and indexed using SAMtools to streamline subsequent analysis. To reduce the impact of PCR duplicates, duplicate reads were marked and removed. Normalized coverage tracks were generated using the bamCoverage command from deepTools, applying RPKM normalization to account for differences in sequencing depth and facilitate direct comparisons between samples. Peak calling was conducted with MACS2 ($q < 0.05$), employing narrow peak detection for histone marks such as H3K4me3 and H3K27Ac, and broad peak detection for marks like H3K9me3, H3K4me1, and H3K79me2. Input DNA served as a control during peak calling. Heatmaps were generated using deepTools. Chromatin states were identified using ChromHMM to define combinatorial chromatin state patterns based on the histone modifications studied(Ernst and Kellis, 2012). ChIP-seq peaks were annotated using ChIPseeker, and super-enhancers were identified with HOMER based on H3K4me1 and H3K27Ac ChIP-seq signals.

Statistics and reproducibility

GraphPad 8 software and R were used for statistical analysis. Results were represented as means ± standard deviations (SDs). The normality of the population distribution will be assessed by Shapiro-Wilk test (a significance level of $\alpha = 0.05$) followed by visualizing with Q-Q plot or histogram. For *in vitro* studies, statistical significance between groups was performed by using an unpaired Student's t-test with a minimum of three biologically independent samples. For *in vivo* studies, between-group differences were assessed using the Mann-Whitney U test as a nonparametric method with a minimum of five biologically independent samples. Statistical significance was determined when p value was less than 0.05.

699 **References**

700 Abdella, R., Talyzina, A., Chen, S., Inouye, C.J., Tjian, R., and He, Y. (2021). Structure of the
701 human Mediator-bound transcription preinitiation complex. Science *372*, 52-56.
702 Alam, H., Tang, M., Maitituoheti, M., Dhar, S.S., Kumar, M., Han, C.Y., Ambati, C.R., Amin,
703 S.B., Gu, B., Chen, T.Y., *et al.* (2020). KMT2D Deficiency Impairs Super-Enhancers to Confer a
704 Glycolytic Vulnerability in Lung Cancer. Cancer Cell *37*, 599-617 e597.
705 Allen, B.L., and Taatjes, D.J. (2015). The Mediator complex: a central integrator of transcription.
706 Nat Rev Mol Cell Biol *16*, 155-166.
707 Anders, S., Pyl, P.T., and Huber, W. (2015). HTSeq--a Python framework to work with high-
708 throughput sequencing data. Bioinformatics *31*, 166-169.
709 Aslakson, C.J., and Miller, F.R. (1992). Selective events in the metastatic process defined by
710 analysis of the sequential dissemination of subpopulations of a mouse mammary tumor. Cancer
711 Res *52*, 1399-1405.
712 Bae, S.Y., Kim, H.J., Lee, K.J., and Lee, K. (2015). Translationally controlled tumor protein
713 induces epithelial to mesenchymal transition and promotes cell migration, invasion and
714 metastasis. Sci Rep *5*, 8061.
715 Barbieri, C.E., Baca, S.C., Lawrence, M.S., Demichelis, F., Blattner, M., Theurillat, J.P., White,
716 T.A., Stojanov, P., Van Allen, E., Stransky, N., *et al.* (2012). Exome sequencing identifies
717 recurrent SPOP, FOXA1 and MED12 mutations in prostate cancer. Nat Genet *44*, 685-689.
718 Barkan, D., El Touny, L.H., Michalowski, A.M., Smith, J.A., Chu, I., Davis, A.S., Webster, J.D.,
719 Hoover, S., Simpson, R.M., Gauldie, J., *et al.* (2010). Metastatic growth from dormant cells
720 induced by a col-I-enriched fibrotic environment. Cancer Res *70*, 5706-5716.
721 Barski, A., Cuddapah, S., Cui, K., Roh, T.Y., Schones, D.E., Wang, Z., Wei, G., Chepelev, I.,
722 and Zhao, K. (2007). High-resolution profiling of histone methylations in the human genome.
723 Cell *129*, 823-837.
724 Berry, D.A., Cronin, K.A., Plevritis, S.K., Fryback, D.G., Clarke, L., Zelen, M., Mandelblatt,
725 J.S., Yakovlev, A.Y., Habbema, J.D., Feuer, E.J., *et al.* (2005). Effect of screening and adjuvant
726 therapy on mortality from breast cancer. N Engl J Med *353*, 1784-1792.
727 Buenrostro, J.D., Giresi, P.G., Zaba, L.C., Chang, H.Y., and Greenleaf, W.J. (2013).
728 Transposition of native chromatin for fast and sensitive epigenomic profiling of open chromatin,
729 DNA-binding proteins and nucleosome position. Nat Methods *10*, 1213-1218.
730 Calvo, F., Ege, N., Grande-Garcia, A., Hooper, S., Jenkins, R.P., Chaudhry, S.I., Harrington, K.,
731 Williamson, P., Moeendarbary, E., Charras, G., *et al.* (2013). Mechanotransduction and YAP-
732 dependent matrix remodelling is required for the generation and maintenance of cancer-
733 associated fibroblasts. Nat Cell Biol *15*, 637-646.
734 Case, L.B., and Waterman, C.M. (2015). Integration of actin dynamics and cell adhesion by a
735 three-dimensional, mechanosensitive molecular clutch. Nat Cell Biol *17*, 955-963.
736 Cerami, E., Gao, J., Dogrusoz, U., Gross, B.E., Sumer, S.O., Aksoy, B.A., Jacobsen, A., Byrne,
737 C.J., Heuer, M.L., Larsson, E., *et al.* (2012). The cBio cancer genomics portal: an open platform
738 for exploring multidimensional cancer genomics data. Cancer Discov *2*, 401-404.
739 Cheng, L., Zhang, X., Wang, Y., Gan, H., Xu, X., Lv, X., Hua, X., Que, J., Ordog, T., and
740 Zhang, Z. (2019). Chromatin Assembly Factor 1 (CAF-1) facilitates the establishment of
741 facultative heterochromatin during pluripotency exit. Nucleic Acids Res *47*, 11114-11131.
742 Cordenonsi, M., Zanconato, F., Azzolin, L., Forcato, M., Rosato, A., Frasson, C., Inui, M.,
743 Montagner, M., Parenti, A.R., Poletti, A., *et al.* (2011). The Hippo transducer TAZ confers
744 cancer stem cell-related traits on breast cancer cells. Cell *147*, 759-772.

745 De Cock, J.M., Shibue, T., Dongre, A., Keckesova, Z., Reinhardt, F., and Weinberg, R.A.
746 (2016). Inflammation Triggers Zeb1-Dependent Escape from Tumor Latency. Cancer Res *76*,
747 6778-6784.
748 Di Martino, J.S., Nobre, A.R., Mondal, C., Taha, I., Farias, E.F., Fertig, E.J., Naba, A., Aguirre-
749 Ghiso, J.A., and Bravo-Cordero, J.J. (2022). A tumor-derived type III collagen-rich ECM niche
750 regulates tumor cell dormancy. Nat Cancer *3*, 90-107.
751 Dobin, A., Davis, C.A., Schlesinger, F., Drenkow, J., Zaleski, C., Jha, S., Batut, P., Chaisson,
752 M., and Gingeras, T.R. (2013). STAR: ultrafast universal RNA-seq aligner. Bioinformatics *29*,
753 15-21.
754 Dupont, S., Morsut, L., Aragona, M., Enzo, E., Giulitti, S., Cordenonsi, M., Zanconato, F., Le
755 Digabel, J., Forcato, M., Bicciato, S.*, et al.* (2011). Role of YAP/TAZ in mechanotransduction.
756 Nature *474*, 179-183.
757 Early Breast Cancer Trialists' Collaborative, G. (2005). Effects of chemotherapy and hormonal
758 therapy for early breast cancer on recurrence and 15-year survival: an overview of the
759 randomised trials. Lancet *365*, 1687-1717.
760 Egeblad, M., Rasch, M.G., and Weaver, V.M. (2010). Dynamic interplay between the collagen
761 scaffold and tumor evolution. Curr Opin Cell Biol *22*, 697-706.
762 El Khattabi, L., Zhao, H., Kalchschmidt, J., Young, N., Jung, S., Van Blerkom, P., Kieffer-
763 Kwon, P., Kieffer-Kwon, K.R., Park, S., Wang, X.*, et al.* (2019). A Pliable Mediator Acts as a
764 Functional Rather Than an Architectural Bridge between Promoters and Enhancers. Cell *178*,
765 1145-1158 e1120.
766 Ernst, J., and Kellis, M. (2010). Discovery and characterization of chromatin states for
767 systematic annotation of the human genome. Nat Biotechnol *28*, 817-825.
768 Ernst, J., and Kellis, M. (2012). ChromHMM: automating chromatin-state discovery and
769 characterization. Nat Methods *9*, 215-216.
770 Esnault, C., Stewart, A., Gualdrini, F., East, P., Horswell, S., Matthews, N., and Treisman, R.
771 (2014). Rho-actin signaling to the MRTF coactivators dominates the immediate transcriptional
772 response to serum in fibroblasts. Genes Dev *28*, 943-958.
773 Foster, C.T., Gualdrini, F., and Treisman, R. (2017). Mutual dependence of the MRTF-SRF and
774 YAP-TEAD pathways in cancer-associated fibroblasts is indirect and mediated by cytoskeletal
775 dynamics. Genes Dev *31*, 2361-2375.
776 Gao, H., Chakraborty, G., Lee-Lim, A.P., Mavrakis, K.J., Wendel, H.G., and Giancotti, F.G.
777 (2014). Forward genetic screens in mice uncover mediators and suppressors of metastatic
778 reactivation. Proc Natl Acad Sci U S A *111*, 16532-16537.
779 Gao, H., Chakraborty, G., Lee-Lim, A.P., Mo, Q., Decker, M., Vonica, A., Shen, R., Brogi, E.,
780 Brivanlou, A.H., and Giancotti, F.G. (2012). The BMP inhibitor Coco reactivates breast cancer
781 cells at lung metastatic sites. Cell *150*, 764-779.
782 Gao, H., Chakraborty, G., Zhang, Z., Akalay, I., Gadiya, M., Gao, Y., Sinha, S., Hu, J., Jiang, C.,
783 Akram, M.*, et al.* (2016). Multi-organ Site Metastatic Reactivation Mediated by Non-canonical
784 Discoidin Domain Receptor 1 Signaling. Cell *166*, 47-62.
785 Gao, J., Aksoy, B.A., Dogrusoz, U., Dresdner, G., Gross, B., Sumer, S.O., Sun, Y., Jacobsen, A.,
786 Sinha, R., Larsson, E.*, et al.* (2013). Integrative analysis of complex cancer genomics and
787 clinical profiles using the cBioPortal. Sci Signal *6*, pl1.
788 Giancotti, F.G. (2013). Mechanisms governing metastatic dormancy and reactivation. Cell *155*,
789 750-764.

790 Guo, Y.E., Manteiga, J.C., Henninger, J.E., Sabari, B.R., Dall'Agnese, A., Hannett, N.M., Spille,
791 J.H., Afeyan, L.K., Zamudio, A.V., Shrinivas, K., *et al.* (2019). Pol II phosphorylation regulates
792 a switch between transcriptional and splicing condensates. Nature *572*, 543-548.
793 Gyorffy, B., Lanczky, A., Eklund, A.C., Denkert, C., Budczies, J., Li, Q., and Szallasi, Z. (2010).
794 An online survival analysis tool to rapidly assess the effect of 22,277 genes on breast cancer
795 prognosis using microarray data of 1,809 patients. Breast Cancer Res Treat *123*, 725-731.
796 Hnisz, D., Abraham, B.J., Lee, T.I., Lau, A., Saint-Andre, V., Sigova, A.A., Hoke, H.A., and
797 Young, R.A. (2013). Super-enhancers in the control of cell identity and disease. Cell *155*, 934-
798 947.
799 Hosseini, H., Obradovic, M.M.S., Hoffmann, M., Harper, K.L., Sosa, M.S., Werner-Klein, M.,
800 Nanduri, L.K., Werno, C., Ehrl, C., Maneck, M., *et al.* (2016). Early dissemination seeds
801 metastasis in breast cancer. Nature *540*, 552-558.
802 Hu, Z., Li, Z., Ma, Z., and Curtis, C. (2020). Multi-cancer analysis of clonality and the timing of
803 systemic spread in paired primary tumors and metastases. Nat Genet *52*, 701-708.
804 Ishihara, S., and Haga, H. (2022). Matrix Stiffness Contributes to Cancer Progression by
805 Regulating Transcription Factors. Cancers (Basel) *14*.
806 Ito, M., Yuan, C.X., Okano, H.J., Darnell, R.B., and Roeder, R.G. (2000). Involvement of the
807 TRAP220 component of the TRAP/SMCC coactivator complex in embryonic development and
808 thyroid hormone action. Mol Cell *5*, 683-693.
809 Joung, J., Konermann, S., Gootenberg, J.S., Abudayyeh, O.O., Platt, R.J., Brigham, M.D.,
810 Sanjana, N.E., and Zhang, F. (2017). Genome-scale CRISPR-Cas9 knockout and transcriptional
811 activation screening. Nat Protoc *12*, 828-863.
812 Kechagia, J.Z., Ivaska, J., and Roca-Cusachs, P. (2019). Integrins as biomechanical sensors of
813 the microenvironment. Nat Rev Mol Cell Biol *20*, 457-473.
814 Keenan, A.B., Torre, D., Lachmann, A., Leong, A.K., Wojciechowicz, M.L., Utti, V., Jagodnik,
815 K.M., Kropiwnicki, E., Wang, Z., and Ma'ayan, A. (2019). ChEA3: transcription factor
816 enrichment analysis by orthogonal omics integration. Nucleic Acids Res *47*, W212-W224.
817 Kubo, N., Chen, P.B., Hu, R., Ye, Z., Sasaki, H., and Ren, B. (2024). H3K4me1 facilitates
818 promoter-enhancer interactions and gene activation during embryonic stem cell differentiation.
819 Mol Cell *84*, 1742-1752 e1745.
820 Lambert, A.W., Pattabiraman, D.R., and Weinberg, R.A. (2017). Emerging Biological Principles
821 of Metastasis. Cell *168*, 670-691.
822 Lefebvre, C., Bachelot, T., Filleron, T., Pedrero, M., Campone, M., Soria, J.C., Massard, C.,
823 Levy, C., Arnedos, M., Lacroix-Triki, M., *et al.* (2016). Mutational Profile of Metastatic Breast
824 Cancers: A Retrospective Analysis. PLoS Med *13*, e1002201.
825 Li, C., Qiu, S., Liu, X., Guo, F., Zhai, J., Li, Z., Deng, L., Ge, L., Qian, H., Yang, L., *et al.*
826 (2023). Extracellular matrix-derived mechanical force governs breast cancer cell stemness and
827 quiescence transition through integrin-DDR signaling. Signal Transduct Target Ther *8*, 247.
828 Liu, X., Ye, Y., Zhu, L., Xiao, X., Zhou, B., Gu, Y., Si, H., Liang, H., Liu, M., Li, J., *et al.*
829 (2023). Niche stiffness sustains cancer stemness via TAZ and NANOG phase separation. Nat
830 Commun *14*, 238.
831 Love, M.I., Huber, W., and Anders, S. (2014). Moderated estimation of fold change and
832 dispersion for RNA-seq data with DESeq2. Genome Biol *15*, 550.
833 Malanchi, I., Santamaria-Martinez, A., Susanto, E., Peng, H., Lehr, H.A., Delaloye, J.F., and
834 Huelsken, J. (2011). Interactions between cancer stem cells and their niche govern metastatic
835 colonization. Nature *481*, 85-89.

836 Mieczkowski, J., Cook, A., Bowman, S.K., Mueller, B., Alver, B.H., Kundu, S., Deaton, A.M.,
837 Urban, J.A., Larschan, E., Park, P.J., *et al.* (2016). MNase titration reveals differences between
838 nucleosome occupancy and chromatin accessibility. Nat Commun *7*, 11485.
839 Nguyen-Ngoc, K.V., Shamir, E.R., Huebner, R.J., Beck, J.N., Cheung, K.J., and Ewald, A.J.
840 (2015). 3D culture assays of murine mammary branching morphogenesis and epithelial invasion.
841 Methods Mol Biol *1189*, 135-162.
842 Obenauf, A.C., and Massague, J. (2015). Surviving at a Distance: Organ-Specific Metastasis.
843 Trends Cancer *1*, 76-91.
844 Pastushenko, I., and Blanpain, C. (2019). EMT Transition States during Tumor Progression and
845 Metastasis. Trends Cell Biol *29*, 212-226.
846 Paszek, M.J., Zahir, N., Johnson, K.R., Lakins, J.N., Rozenberg, G.I., Gefen, A., Reinhart-King,
847 C.A., Margulies, S.S., Dembo, M., Boettiger, D., *et al.* (2005). Tensional homeostasis and the
848 malignant phenotype. Cancer Cell *8*, 241-254.
849 Pelossof, R., Fairchild, L., Huang, C.H., Widmer, C., Sreedharan, V.T., Sinha, N., Lai, D.Y.,
850 Guan, Y., Premsrirut, P.K., Tschaharganeh, D.F., *et al.* (2017). Prediction of potent shRNAs with
851 a sequential classification algorithm. Nat Biotechnol *35*, 350-353.
852 Posern, G., and Treisman, R. (2006). Actin' together: serum response factor, its cofactors and the
853 link to signal transduction. Trends Cell Biol *16*, 588-596.
854 Reddy, K.L., Zullo, J.M., Bertolino, E., and Singh, H. (2008). Transcriptional repression
855 mediated by repositioning of genes to the nuclear lamina. Nature *452*, 243-247.
856 Reya, T., and Clevers, H. (2005). Wnt signalling in stem cells and cancer. Nature *434*, 843-850.
857 Rueda, O.M., Sammut, S.J., Seoane, J.A., Chin, S.F., Caswell-Jin, J.L., Callari, M., Batra, R.,
858 Pereira, B., Bruna, A., Ali, H.R., *et al.* (2019). Dynamics of breast-cancer relapse reveal late-
859 recurring ER-positive genomic subgroups. Nature *567*, 399-404.
860 Siegel, M.B., He, X., Hoadley, K.A., Hoyle, A., Pearce, J.B., Garrett, A.L., Kumar, S., Moylan,
861 V.J., Brady, C.M., Van Swearingen, A.E., *et al.* (2018). Integrated RNA and DNA sequencing
862 reveals early drivers of metastatic breast cancer. J Clin Invest *128*, 1371-1383.
863 Soutourina, J. (2018). Transcription regulation by the Mediator complex. Nat Rev Mol Cell Biol
864 *19*, 262-274.
865 Stevens, J.L., Cantin, G.T., Wang, G., Shevchenko, A., Shevchenko, A., and Berk, A.J. (2002).
866 Transcription control by E1A and MAP kinase pathway via Sur2 mediator subunit. Science *296*,
867 755-758.
868 Subramanian, A., Tamayo, P., Mootha, V.K., Mukherjee, S., Ebert, B.L., Gillette, M.A.,
869 Paulovich, A., Pomeroy, S.L., Golub, T.R., Lander, E.S., *et al.* (2005). Gene set enrichment
870 analysis: a knowledge-based approach for interpreting genome-wide expression profiles. Proc
871 Natl Acad Sci U S A *102*, 15545-15550.
872 Sun, F., Sun, T., Kronenberg, M., Tan, X., Huang, C., and Carey, M.F. (2021). The Pol II
873 preinitiation complex (PIC) influences Mediator binding but not promoter-enhancer looping.
874 Genes Dev *35*, 1175-1189.
875 Terranova, C., Tang, M., Orouji, E., Maitituoheti, M., Raman, A., Amin, S., Liu, Z., and Rai, K.
876 (2018). An Integrated Platform for Genome-wide Mapping of Chromatin States Using High-
877 throughput ChIP-sequencing in Tumor Tissues. J Vis Exp.
878 Tsherniak, A., Vazquez, F., Montgomery, P.G., Weir, B.A., Kryukov, G., Cowley, G.S., Gill, S.,
879 Harrington, W.F., Pantel, S., Krill-Burger, J.M., *et al.* (2017). Defining a Cancer Dependency
880 Map. Cell *170*, 564-576 e516.

881 Turajlic, S., and Swanton, C. (2016). Metastasis as an evolutionary process. Science *352*, 169-
882 175.
883 Ueno, H., Shinto, E., Hashiguchi, Y., Shimazaki, H., Kajiwara, Y., Sueyama, T., Yamamoto, J.,
884 and Hase, K. (2015). In rectal cancer, the type of desmoplastic response after preoperative
885 chemoradiotherapy is associated with prognosis. Virchows Arch *466*, 655-663.
886 van Steensel, B., and Belmont, A.S. (2017). Lamina-Associated Domains: Links with
887 Chromosome Architecture, Heterochromatin, and Gene Repression. Cell *169*, 780-791.
888 Verger, A., Monte, D., and Villeret, V. (2019). Twenty years of Mediator complex structural
889 studies. Biochem Soc Trans *47*, 399-410.
890 Werner-Klein, M., Grujovic, A., Irlbeck, C., Obradovic, M., Hoffmann, M., Koerkel-Qu, H., Lu,
891 X., Treitschke, S., Kostler, C., Botteron, C.*, et al.* (2020). Interleukin-6 trans-signaling is a
892 candidate mechanism to drive progression of human DCCs during clinical latency. Nat Commun
893 *11*, 4977.
894 Whyte, W.A., Orlando, D.A., Hnisz, D., Abraham, B.J., Lin, C.Y., Kagey, M.H., Rahl, P.B., Lee,
895 T.I., and Young, R.A. (2013). Master transcription factors and mediator establish super-
896 enhancers at key cell identity genes. Cell *153*, 307-319.
897 Wreggett, K.A., Hill, F., James, P.S., Hutchings, A., Butcher, G.W., and Singh, P.B. (1994). A
898 mammalian homologue of Drosophila heterochromatin protein 1 (HP1) is a component of
899 constitutive heterochromatin. Cytogenet Cell Genet *66*, 99-103.
900 Zhang, X.H., Giuliano, M., Trivedi, M.V., Schiff, R., and Osborne, C.K. (2013). Metastasis
901 dormancy in estrogen receptor-positive breast cancer. Clin Cancer Res *19*, 6389-6397.
902 Zhao, B., Ye, X., Yu, J., Li, L., Li, W., Li, S., Yu, J., Lin, J.D., Wang, C.Y., Chinnaiyan, A.M.*,*
903 *et al.* (2008). TEAD mediates YAP-dependent gene induction and growth control. Genes Dev
904 *22*, 1962-1971.
905

Acknowledgements

This study is dedicated to the memory of our mentor, teacher, and friend, Filippo Giancotti, a pioneer in the metastasis field known for his brilliance, rigor, and kindness. This work was supported by NIH grant R35 CA197566 and partially by CPRIT Recruitment of Established Investigators Award RR160031 (F.G.G.). Use of the Core Facilities was supported by NIH grants P30 CA008748 (MSKCC), P30 CA016672 (MDACC), and P30 CA013696 (Columbia University).

Author contributions

S.-Y.B. designed the project and performed most of experiments. F.G.G directed the project and provided supervision. S.-Y.B., Y.C., and H.C. performed bioinformatic analyses. D.K. helped in some of the experiments of RT-qPCR, and data analysis. S.-Y.B., A.D.V., R.A.D. were responsible for data analysis and their interpretation. S.-Y.B., A.D.V. and R.A.D. wrote the manuscript.

Competing interests

R.A.D. is founder, advisor and/or director of Tvardi Therapeutics, Inc., Bectas Therapeutics, Inc., and Asylia Therapeutics, Inc., and a limited partner of Sporos Bioventures, LLC. The work of these entities is not related to the science of this manuscript. A.D.V is in the scientific advisory board for Arima Genomics. All other authors declare no competing interests.

Materials & Correspondence

Correspondence and requests for materials should be addressed to Seong-Yeon Bae (S.-Y.B.) and Ronald A. DePinho (R.A.D)

926 **Figure Legends**

927 **Figure 1 *Med4* was identified as a gatekeeper for metastatic reactivation by forward genetic**
928 **screening using CRISPR-Cas9 system. (A)** Schematic representation of the *in vivo* CRISPR-
929 Cas9 screening strategy. **(B)** Schematic overview of the screening and validation process. The flow
930 diagram outlines the progressive filtering and validation steps leading to the identification of the
931 most promising target, Med4. **(C),** RT-qPCR analysis and immunoblots of *Med4* expression in
932 D2A1-d-TGL cells expressing MirE shRNA targeting either non-targeting control (NTC) or *Med4.*
933 RhoGDI was served as the loading control.; Mean values (± S.D.), p values; unpaired Student's t-
934 test. **(D-F),** D2A1-d-TGL cells transduced with either NTC or *Med4* shRNAs were inoculated *i.v.*
935 in syngeneic mice. Lung metastasis was measured by bioluminescent (BLI) imaging at the
936 indicated time. The panels show representative images (D), the graphs of the normalized BLI
937 photon flux (E), and the graphs of the counts of macrometastases (F). Mean values (± S.D.), p
938 values; Mann-Whitney U test (E and F). **(G-J)** Schematic representation of inducible expression
939 experiment (G), Immunoblot analysis of MED4 in D2A1-d-TGL cells transduced with
940 doxycycline (Dox)-inducible MirE shRNA targeting NTC or *Med4*. RhoGDI was served as the
941 loading control. (H), D2A1-d-TGL cells expressing Dox-inducible MirE shRNA targeting NTC
942 or *Med4* were inoculated *i.v.* in syngeneic mice. Dox was administrated either immediately after
943 injection (Dox day 0) or 14 days after inoculation of the cells (Dox day 14). Lung metastasis was
944 measured by BLI normalized photon flux at the indicated time. The panels show representative
945 images (I), and the graphs of the normalized BLI photon flux (J); Mean values (± S.D.) p values;
946 Mann-Whitney U test. **(K-M)** D2A1-d-TGL cells expressing shRNA targeting either non-targeting
947 control (NTC) or *Med4* were inoculated intracardially (i.c.) in syngeneic mice. Representative BLI
948 images of mice at indicated time points (K) and *ex vivo* BLI images of forelimb and hind limb
949 bones (L) were captured. Bone sections were subjected to H&E staining and TRAP staining (M),
950 with arrows indicating osteolytic bone lesions.

951 **Figure 2 *Med4* inhibits the reprogramming of the transcriptional and epigenetic landscape**
952 **to suppress matrix stiffening. (A)** Heatmap of differentially expressed genes (DEGs; |Fold
953 change| ≥ 2, FDR < 0.05) in NTC versus *Med4*-silenced D2A1-d-TGL one week after transduction.
954 **(B)** Differential accessibility ($\log_2$ fold change in reads per accessible region) plotted against the
955 mean reads per region. **(C)** D2A1-d cells expressing either NTC or *Med4* shRNAs were stained
956 with HP1α (red). The panels display representative images (left) and a violin plot showing the ratio
957 of heterochromatin foci puncta area to nuclear area (right). The data were obtained by measuring
958 the area of heterochromatin puncta and nuclear area using ImageJ. Statistical significance was
959 assessed using an unpaired t-test. **(D)** Intersection of RNA-seq and ATAC-seq plotted as -
960 $\log_{10}$(FDR)*sign of the $\log_2$ fold change of *Med4*-sileced D2A1-d-TGL cells compared to NTC
961 and each point representing one ATAC peak. **(E)** Gene ontology (GO) analysis of the genes located
962 in the upper quadrant of (D) from the intersection of RNA-seq and ATAC-seq. **(F)** Heatmap shows
963 the expression level of matrisome genes amongst the top differentially expressed genes in NTC
964 versus *Med4*-depleted cells. **(G)** Metagene plots displaying ATAC-seq signal at promoter regions
965 (around transcription start sites (TSS) within ±3 kb) for upregulated DEGs (Up DEGs),
966 downregulated DEGs (Down DEGs), and non-affected genes (top). Violin plots showing the
967 distribution of RPKM values for chromatin accessibility at promoter regions. Wilcoxon rank-sum
968 test was used for statistical analysis (bottom). **(H)** IGV tracks showing ATAC-seq and RNA-seq
969 profiles for on the *Acta2* and *Adamts5* genes in NTC and *Med4*-depleted D2A1-d-TGL cells. The
970 promoter regions are highlighted in red. **(I)** Immunohistochemistry for α-SMA and Masson's

971 trichrome staining on lung metastases in mice that were intravenously injected with D2A1-d-TGL
972 cells transduced with either non-targeting control (NTC) or *Med4* shRNAs.

973 **Figure 3 *Med4* maintains enhancer poise, restricting abnormal ECM gene expression. (A)**
974 Emission probabilities of the 10-state ChromHMM model on the basis of ChIP-seq profiles of five
975 histone marks (shown in x axis) profiles in D2A1-d cells expressing MirE shRNA targeting *Med4*
976 or NTC. Each row represents one chromatin state, and each column corresponds to one chromatin
977 mark. The 10 states predicted using ChromHMM represent various enhancer states (E05, E06, E07,
978 E08, and E09), promoter state (E03 and E04), transcription states (E10), and heterochromatin state
979 (E02). Each column corresponds to a histone modification. **(B)** The top GO cellular component
980 terms in active enhancer (E06; upper) states and poised enhancer (E07; bottom). **(C)** Heatmaps
981 showing H3K4me1 and H3K27Ac across the individual peaks of distal enhancer chromatin states
982 **(D)** Metagene plot of mean ChIP-seq signal of H3K4me1, H3K27ac and ATAC-seq signal across
983 the individual peaks of each mark. Metagene analysis was centered on the middle of peaks and 4
984 kb around peak centers are displayed (2 kb upstream and 2 kb downstream). **(E)** Distribution of
985 normalized H3K4me1 signal enrichment across enhancer regions in NTC (left) and Med4-silenced
986 cells (right). A subset of regions with exponentially higher levels of H3K4me1 comprises super-
987 enhancers (SEs; red), while the remainder are typical enhancers (TEs; grey). **(F)** The distribution
988 of normalized H3K27Ac signal enrichment across enhancer regions in NTC (left) and Med4-
989 silenced cells (right) similarly identifies SEs (red) and TEs (grey). **(G)** Intersection of H3K4me1-
990 enriched SEs (left) and H3K27Ac-enriched SEs (right) between NTC and shMed4 cells. **(H)**
991 Genome tracks showing H3K4me1-enriched SEs associated with the *Col6a3* gene. The *de novo*
992 SE in sh*Med4* is highlighted in red and the persistent SE is highlighted in yellow.

993 **Figure 4 *Med4* sustains dormancy by suppressing integrin-mediated mechano-transduction.**
994 **(A)** D2A1-d cells expressing MirE shRNA targeting *Med4* or NTC were cultured on 3D Matrigel
995 with or without collagen I. **(B)** D2A1-d cells expressing MirE shRNA targeting Med4 cultured on
996 2D were stained for either vinculin or paxillin (green), F-actin (red), p-FAK (purple) and the nuclei
997 were counterstained with DAPI (blue). Arrows indicate the focal adhesion plaques. **(C)** ChEA3
998 TF enrichment analysis of the promoters of the genes upregulated in *Med4*-depleted cells
999 compared to NTC. **(D)** Gene signature enrichment analysis (GSEA) of MRTF, SRF, and YAP
1000 transcriptional signatures. NES, normalized enrichment score; FDR, false discovery rate (n = 3
1001 biological replicates per condition). **(E)** RT-qPCR results were indicated as relative mean
1002 expression of MRTF/SRF only target genes, YAP only target genes and shared target genes in
1003 either control or *Med4*-depleted D2A1-d cells. **(F)** D2A1-d cells expressing MirE shRNA targeting
1004 *Med4* cultured on 2D were stained for MRTF-A (red), or for YAP (purple). The nuclei were
1005 counterstained with DAPI (blue). **(G)** D2A1-d-TGL cells co-transduced with indicated MirE
1006 shRNAs were inoculated *i.v.* in syngeneic mice. Lung metastasis was measured by bioluminescent
1007 (BLI) imaging at the indicated time. The panels show representative images (left), and the graphs
1008 of the normalized BLI photon flux (right). Mean values (± S.D.) p values; Mann-Whitney U test.

1009 **Figure 5 *MED4* haploinsufficiency and associated haplo-signatures are correlated with**
1010 **metastatic relapse in patients. (A)** Copy number alterations in metastatic breast cancer patients
1011 (from INSERM) were analyzed by cBioportal database. **(B)** *MED4* mRNA levels were measured
1012 by paired RNA-seq of primary tumors and multiple metastases. **(C)** Kaplan-Meier analysis of
1013 relapse-free survival (RFS) of all patients in publicly available breast cancer datasets (source KM
1014 Plotter for breast cancer). **(D)** Patients were stratified according to *MED4* expression using a probe

set, 222438_at as indicated. HR, hazard ratio. Kaplan-Meier curve of the Breast Cancer Meta-base: 10 cohorts 22K gene data showing the distant metastasis-free survival (DMFS) of patients separated in 2 cohorts based on the risk (left). Red and green curves denote high- and low-risk groups respectively. Box plot across risk groups, including the p-value testing for difference using t-test (right). **(E)** Kaplan-Meier analysis of DMFS in patients stratified by the expression of the *MED4*-associated haplo-gene signature. **(F)** Schematic illustration of MED4's role in maintaining the epigenomic landscape and cellular dormancy. *Med4* inhibits enhancer activation (weak to active) and priming (poised to primed) by suppressing H3K4me1 deposition. *Med4* depletion disrupts this control, leading to epigenomic and transcriptional reprogramming that rewires ECM protein and integrin expression, promoting integrin-mediated mechanotransduction. Stress fiber assembly further reinforces chromatin modifications by exerting tension on the nuclear membrane. *Med4* acts as a gatekeeper of dormancy by regulating enhancer dynamics.

1027 **Extended Data Figure Legends**

1028 **Figure S1 *Med4* was heterozygously deleted to induce metastatic reactivation. (A)** 4T07-TGL
1029 cells either mock control or expressing GeCKO v2 library were inoculated *i.v.* into BALB/c
1030 syngeneic mice. Lung metastasis was measured by bioluminescent (BLI) imaging at the indicated
1031 time. **(B)** The scheme of chromatin looping for enhancer-promoter interaction. **(C)** Schematics of
1032 the mouse chromosomal region encompassing *Med4*, location of the sequence complementary to
1033 the gRNA isolated from the screening, and the primer pairs used for genomic DNA PCR. **(D)** The
1034 isolated clone from the screening which harbors a gRNA targeting *Med4* was subjected to an indel
1035 analysis using genomic DNA PCR, electrophoresed in a DNA-PAGE gel (left), and
1036 immunoblotting (right). RhoGDI was served as the loading control. **(E)** Sequences of the
1037 fragments of DNA deleted by CRISPR-Cas9. Red boxes indicate the junction. **(F)** Sequence
1038 alignment results of translated amino acids from each allele to wild type *Med4*. **(G)** DepMap
1039 analysis of the dependency of tumor cell line panels in CRISPR (blue) and RNAi (violet) databases
1040 on *MED4*. X-axis: dependency scores. **(H)** RT-qPCR analysis and immunoblots of *Med4*
1041 expression in 4T07-TGL cells expressing MirE shRNA targeting either non-targeting control
1042 (NTC) or *Med4.* RhoGDI was served as the loading control.; Mean values (± S.D.) p-values;
1043 unpaired Student's t-test. **(I)** 4T07-TGL cells transduced with either NTC or *Med4* shRNAs were
1044 inoculated *i.v.* in syngeneic mice. Lung metastasis was measured by bioluminescent (BLI) imaging
1045 at the indicated time.

1046 **Figure S2 *Med1* alters the transcriptional and epigenetic landscape discordantly with *Med4***
1047 **while *Med4*-happloinsufficiency driven transcriptional program is necessary for metastasis.**
1048 **(A)** MA plot from RNA-seq analysis in D2A1 versus D2A1-d cells (Fold change ≥ 2, FDR < 0.05)
1049 **(B)** GSEA plots of D2A1_metastatic and D2A1_dormant signatures in Med4-depleted cells as
1050 compared with control cells. **(C)** RT-qPCR analysis and immunoblots of *Med1* expression in
1051 D2A1-d-TGL cells expressing MirE shRNA targeting either non-targeting control (NTC) or *Med1*;
1052 Mean values (± S.D.) p values; unpaired Student's t-test. **(D)** Heatmap of differentially expressed
1053 genes (DEGs; Fold change ≥ 2, FDR < 0.05) in NTC versus *Med1*-silenced D2A1-d-TGL cells.
1054 **(E)** GSEA plots of D2A1_metastatic and D2A1_dormant signatures in *Med1*-silenced cells as
1055 compared with control cells. **(F)** MA plot of ATAC-seq results comparing NTC versus *Med1*-
1056 silenced D2A1-d-TGL cells. Differential accessibility ($\log_2$ fold change in reads per accessible
1057 region) plotted against the mean reads per region. **(G and H)** MNase digestion assays were
1058 performed on nuclei isolated from the indicated *Med4*-depleted (G) and *Med1*-depleted (H) cells
1059 over increasing incubation times. The panels display representative images (upper) and
1060 corresponding quantification graphs (lower). **(I)** D2A1-d cells expressing either NTC or *Med1*
1061 shRNAs were stained with HP1α (red). **(J)** ATAC-seq profiles were generated for Up DEGS (up),
1062 Down DEGs (middle), and non-affected DEGs (bottom). The profiles display ATAC-seq signal
1063 from 5 kb upstream of the TSS to 5 kb downstream of the TES, capturing the chromatin
1064 accessibility landscape across gene bodies.

1065 **Figure S3 *Med4* haploinsufficiency induces epigenomic reprogramming, making genome**
1066 **permissive to transcriptional activation. (A-E)** Differential binding sites (FDR < 0.05) were
1067 plotted against the mean reads per region for H3K4me1 (A), H3K27Ac (B), H3K4me3 (C),
1068 H3K79me2 (D), and H3K9me3 (E). **(F-I)** Violin plots illustrating the distribution of RPKM values
1069 for (F), H3K27Ac (G), H3K4me3 (H), and H3K9me3 (I) at each chromatin states defined by
1070 ChromHMM. Wilcoxon rank-sum test was used for statistical analysis. **(J)** The top GO cellular

component terms in promoter (E04), weak enhancer (E05), genic enhancer (E08), and transcription (E10).

Figure S4 *Med4* reduces epigenomic signals at super-enhancers and typical enhancers genome-wide. (A and **B)** Heatmaps (left panels) and average intensity curves (right panels) of ChIP-seq reads (RPKM) for H3K4me1 (A) and H3K27ac (B) at super-enhancer regions, including their flanking 2-kb regions. **(C** and **D)** Heatmaps (left panels) and average intensity curves (right panels) of ChIP-seq reads for H3K4me1 (C) and H3K27ac (D) at typical enhancer regions, displayed within a 10-kb window centered on the middle of the enhancer. **(E and F)** Top 5 GO terms across biological processes (BP), cellular components (CC), and molecular functions (MF) in H3K4me1-enriched super-enhancers (E) and H3K27Ac-enriched super-enhancers (F). Categories are shown for *de novo* super-enhancers in *Med4*-silenced cells (left), persistent super-enhancers shared between *Med4*-silenced and control cells (middle), and lost super-enhancers in *Med4*-silenced cells (right).

Figure S5 *Med4* suppresses cancer stem cell traits in D2A1-d cells. (A) GSEA of KEGG_Wnt signaling pathway signatures. NES, normalized enrichment score; FDR, false discovery rate (n = 3 biological replicates per condition). **(B)** Control or *Med4*-depleted D2A1-d-TGL cells were subjected to tumorsphere assay for 10 days. The panel shows representative images of wells and microscopic images of tumor spheres (left) and mean numbers of organoid (± S.D.; right) per 10,000 cells. p values; unpaired Student's t-test (n = 3 per group, *P = 0.0122, **P = 0.0089). **(C)** Indicated D2A1-d-TGL cells were subjected to clonogenicity assay for 6 days. The panel shows representative images of dishes and microscopic images of colonies (left) and mean numbers of colonies (± S.D.; right) per 1,000 cells. p values; unpaired Student's t-test (n = 3 per group, **P = 0.0056, ***P = 0.0006). **(D)** Indicated D2A1-d-TGL cells were subjected to soft agar assay for 10 days. The panel shows representative images of wells and microscopic images of colonies (left) and mean numbers of colonies (± S.D.; right) per 10,000 cells. p values; unpaired Student's t-test (n = 3 per group, *P = 0.0118, ****P < 0.0001). **(E and F)** Control or *Med4*-silenced D2A1-d-TGL cells were subjected to transwell migration assay (E) and transwell invasion assay (F) for 24 hours. The panel shows representative images of fields (left) and mean numbers of cells (± S.D.; right) per field. p values; unpaired Student's t-test (E**;** n = 3 per group, ***P = 0.0007, ***P = 0.0009, F**;** n = 3 per group, **P = 0.0018, ***P = 0.0007).

Figure S6 *Med4* inhibits cancer stem cell traits in 4T07 cells. (A) Tumorsphere assay results in control and *Med4*-silenced 4T07-TGL cells 10 days post-seeding. The panel shows representative images of wells and microscopic images of tumor spheres (left) and mean numbers of organoid (± S.D.; right) per 10,000 cells. p values; unpaired Student's t-test (n = 3 per group, *P = 0.0158, **P = 0.0055). **(B)** Indicated 4T07-TGL cells were subjected to clonogenicity assay for 6 days. The panel shows representative images of dishes and microscopic images of colonies (left) and mean numbers of colonies (± S.D.; right) per 1,000 cells. p values; unpaired Student's t-test (n = 3 per group, ***P = 0.0002, ****P < 0.0001). **(C)** Soft agar assay results in the indicated 4T07-TGL cells 10 days post-seeding. The panel shows representative images of wells and microscopic images of colonies (left) and mean numbers of colonies (± S.D.; right) per 1,000 cells. p values; unpaired Student's t-test (n = 3 per group, **P = 0.0018, **P = 0.0027). **(D)** Transwell migration results of control and *Med4*-silenced 4T07-TGL cells 24 hours post-seeding. The panel shows representative images of fields (left) and mean numbers of cells (± S.D.; right) per field. p values; unpaired Student's t-test (n = 3 per group, ***P = 0.0001, ****P < 0.0001).

1115 **Figure S7 *Med4* alters the repertoire of integrin subunits and mediates the formation of focal**
1116 **adhesion plaques. (A)** A GSEA plot of integrin complex (GO_CC; top). Heatmap shows the level
1117 of expression of integrin subunit genes amongst the top differentially expressed genes in control
1118 versus *Med4*-silenced D2A1-d-TGL cells (bottom). **(B)** (Individual channel images for Figure 4C)
1119 D2A1-d cells expressing MirE shRNA targeting Med4 cultured on 2D were stained for either
1120 vinculin or paxillin (green), F-actin (red), and the nuclei were counterstained with DAPI (blue).
1121 Arrows highlight focal adhesion plaques. **(C)** Total cell lysates were subjected to immunoblotting
1122 for integrin-signaling molecules. RhoGDI and total ERK, JNK, and p38 were served as internal
1123 loading controls.

1124 **Figure S8 *Med4* mediates the signaling pathway of integrin-mediated mechanotransduction.**
1125 **(A)** HOMER motif analysis of genes in the upper right quadrant of (Figure 3D) which represents
1126 the intersection of RNA-seq and ATAC-seq data in *Med4*-silenced D2A1-d-TGL cells compared
1127 to non-targeting control (NTC). p-values were generated using the binomial test. **(B-F)** Schematic
1128 representation of inducible expression experiment (B), RT-qPCR results were indicated as relative
1129 mean expression of *Med4* (C), MRTF/SRF only target genes (D), shared target genes (E), and
1130 YAP/TEAD only target genes (F) and in either control or *Med4*-silenced D2A1-d cells at the
1131 indicated time points after initiating doxycycline treatment. **(G)** RT-qPCR results were indicated
1132 as relative mean expression of MRTF/SRF only target genes in D2A1-d cells expressing either
1133 NTC or Med4 shRNAs were co-transduced with either empty vector (EV) or Flag-HA tagged
1134 MED4 cDNA. p values; unpaired Student's t-test (n = 3 per group, *P = 0.0449, **P = 0.0016,
1135 ***P = 0.001, ****P < 0.0001). **(H)** D2A1-d cells expressing either NTC or *Med4* shRNAs were
1136 co-transduced with either empty vector (EV) or Flag-HA tagged *MED4* cDNA to rescue MED4
1137 expression. Cells were stained with MRTF-A (red) and counter-stained with DAPI (blue). The
1138 panel shows representative images (left) and quantification of subcellular localization (right). N
1139 stands for the nucleus and C stands for the cytosol. **(I)** D2A1-d-TGL cells were co-transduced with
1140 MirE shRNA targets for *Med4* and MirE shRNA targets the mechanosensitive transcription factors
1141 as indicated. Total lysates were subjected to immunoblotting with the indicated antibodies.
1142 RhoGDI was served as the loading control.

1143 **Figure S9 *MED4* serves as a predictor for breast cancer relapse. (A and B)** cBioportal analysis
1144 of copy number alterations in metastatic breast cancer patients from the Metastatic Breast Cancer
1145 Project; Provisional (A) and Archived (B). **(C)** Kaplan-Meier analysis of RFS in patients stratified
1146 according to *MED4* expression using a probe set, 222438_at as indicated. Patients were subdivided
1147 by breast cancer subtypes according to PAM50. **(D** and **E)** KM plotter analysis of overall survival
1148 (OS) based on *MED4* expression level from RNA-seq data of breast cancer patients. Patients were
1149 subdivided by estrogen receptor (ER) expression level (D) or by human epidermal growth factor
1150 receptor 2 (*HER2*) expression level determined by Affymetrix microarray (E). HR, hazard ratio.

Figure 1 Bae et al.

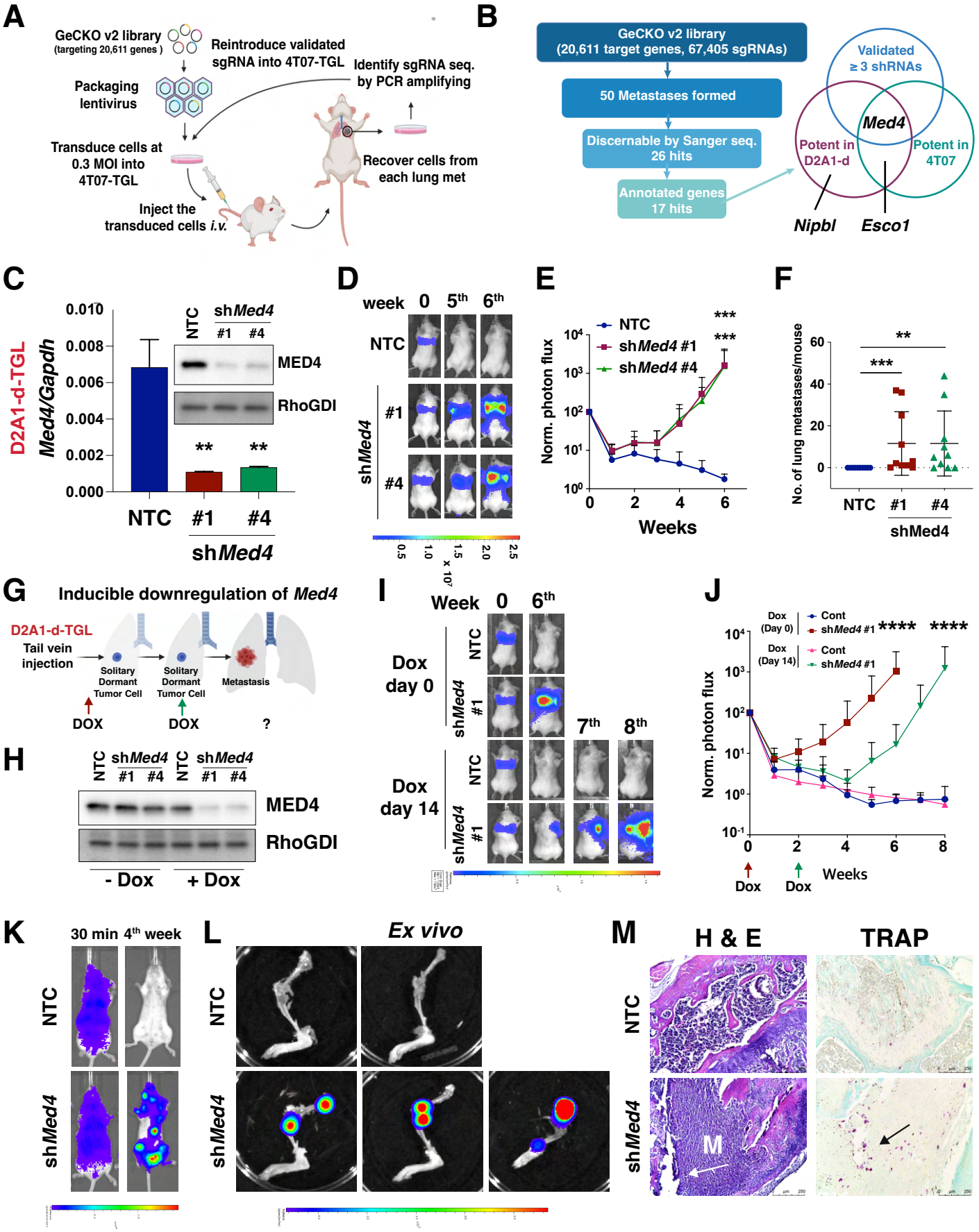

Figure 2 Bae et al.

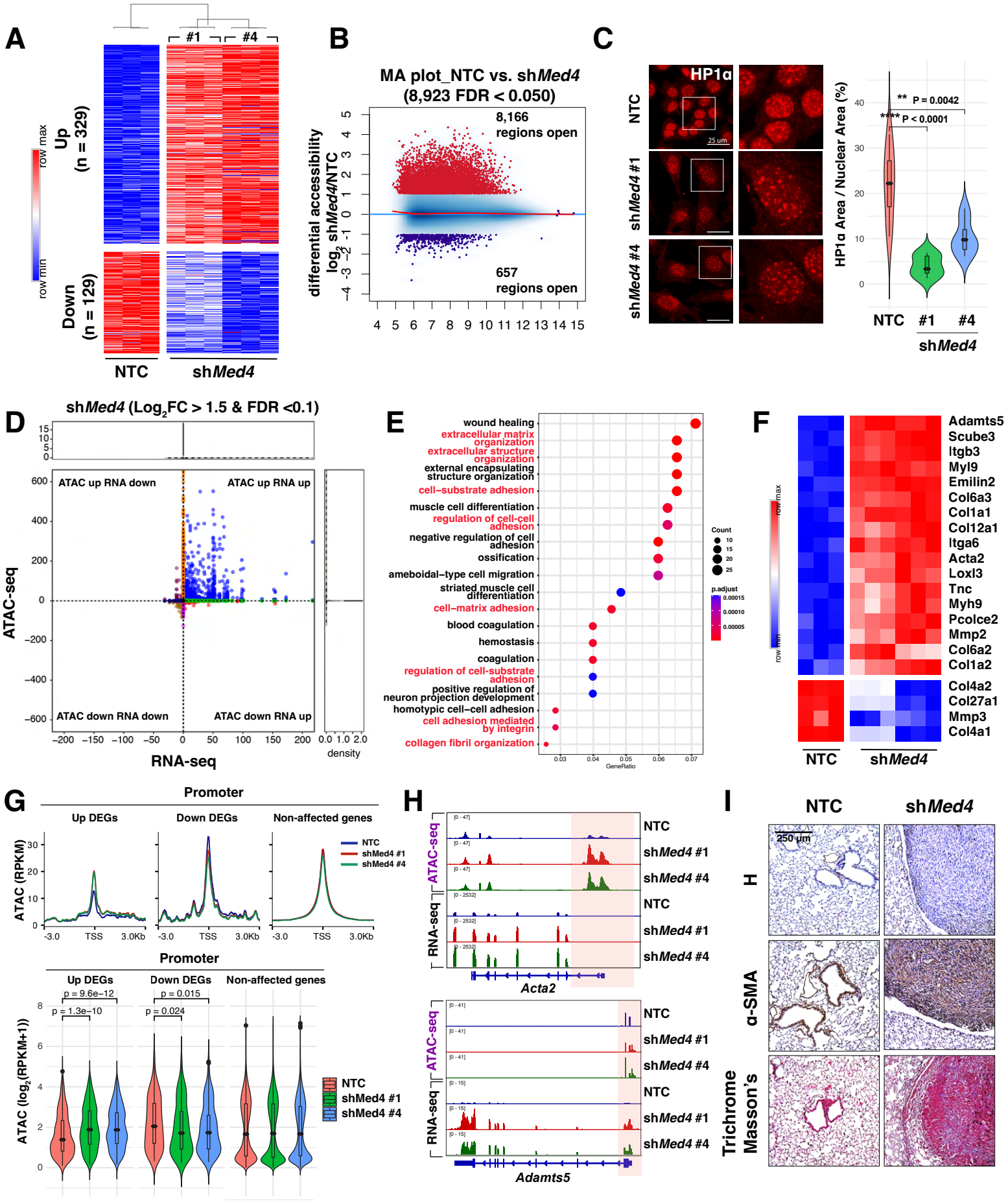

Figure 3 Bae et al.

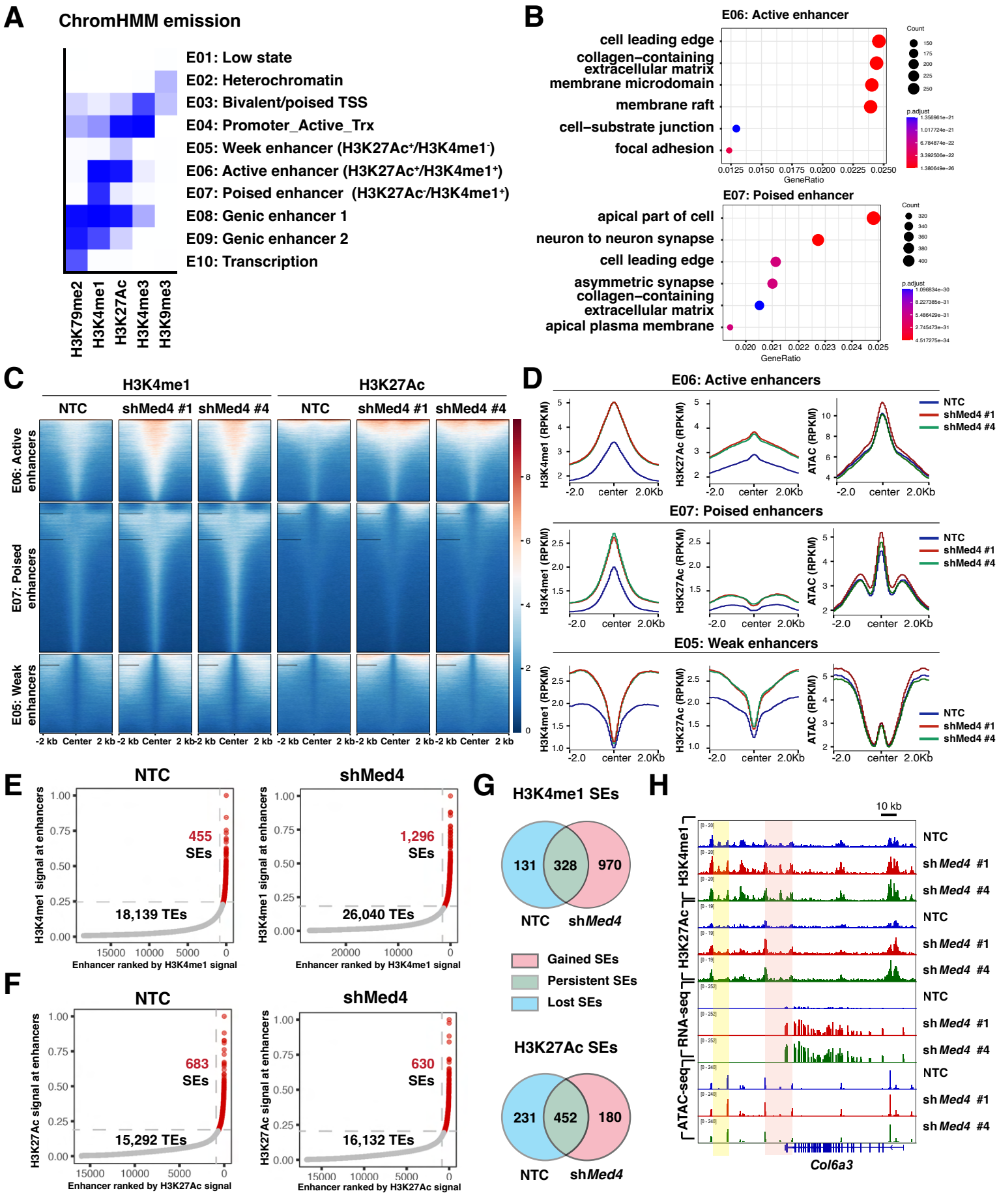

Figure 4 Bae et al.

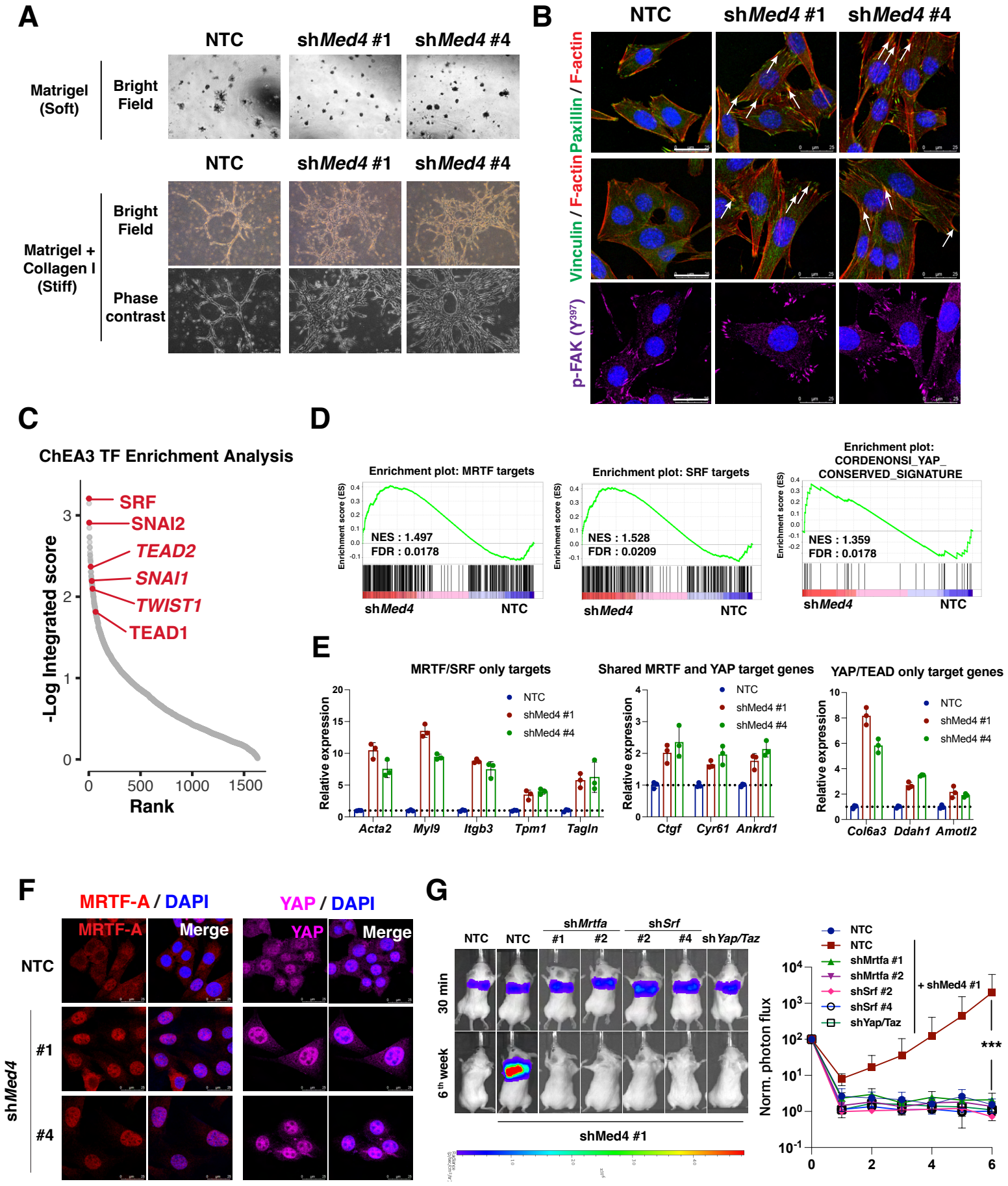

Figure 5 Bae et al.

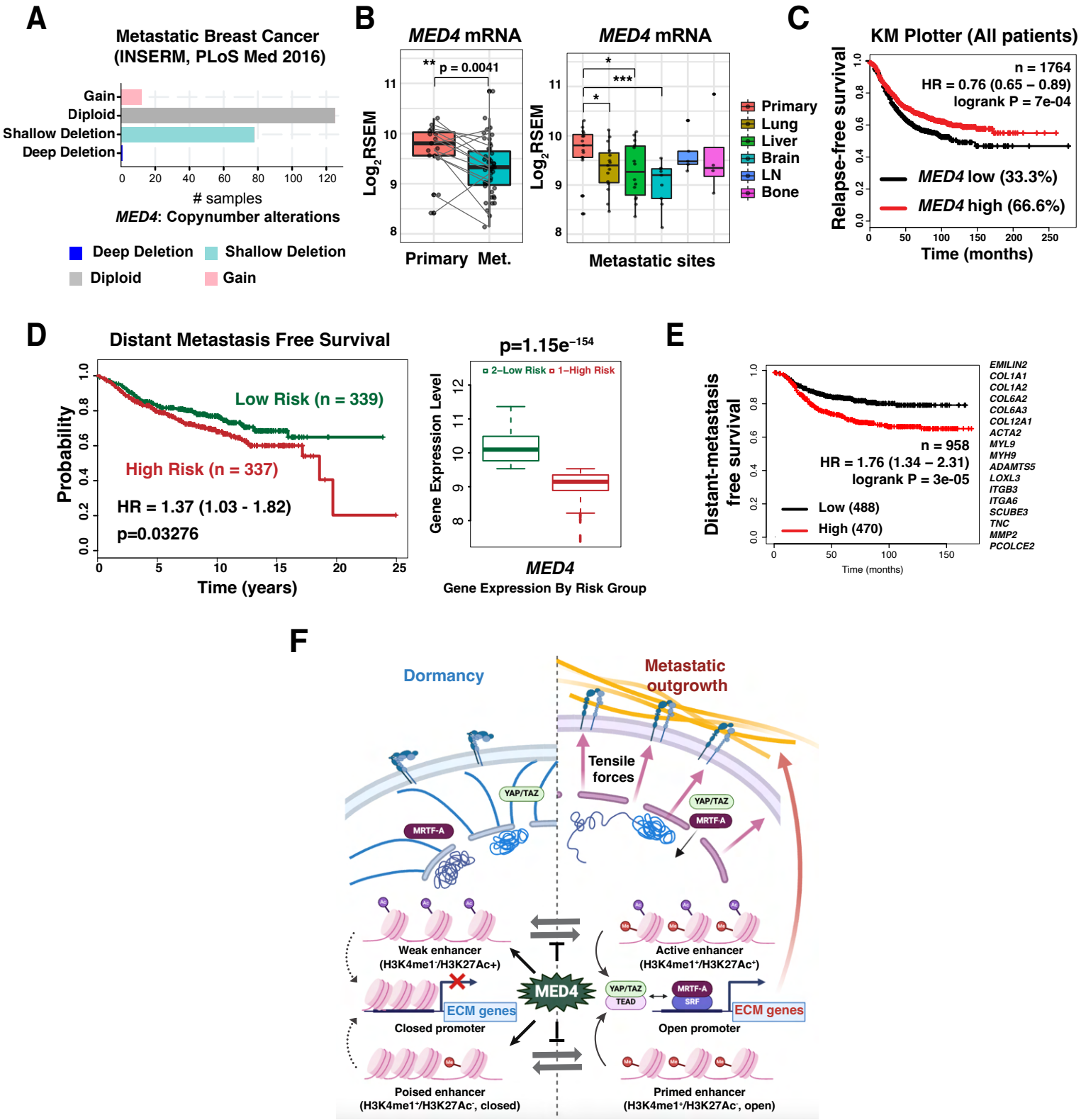

Figure S1 Bae et al.

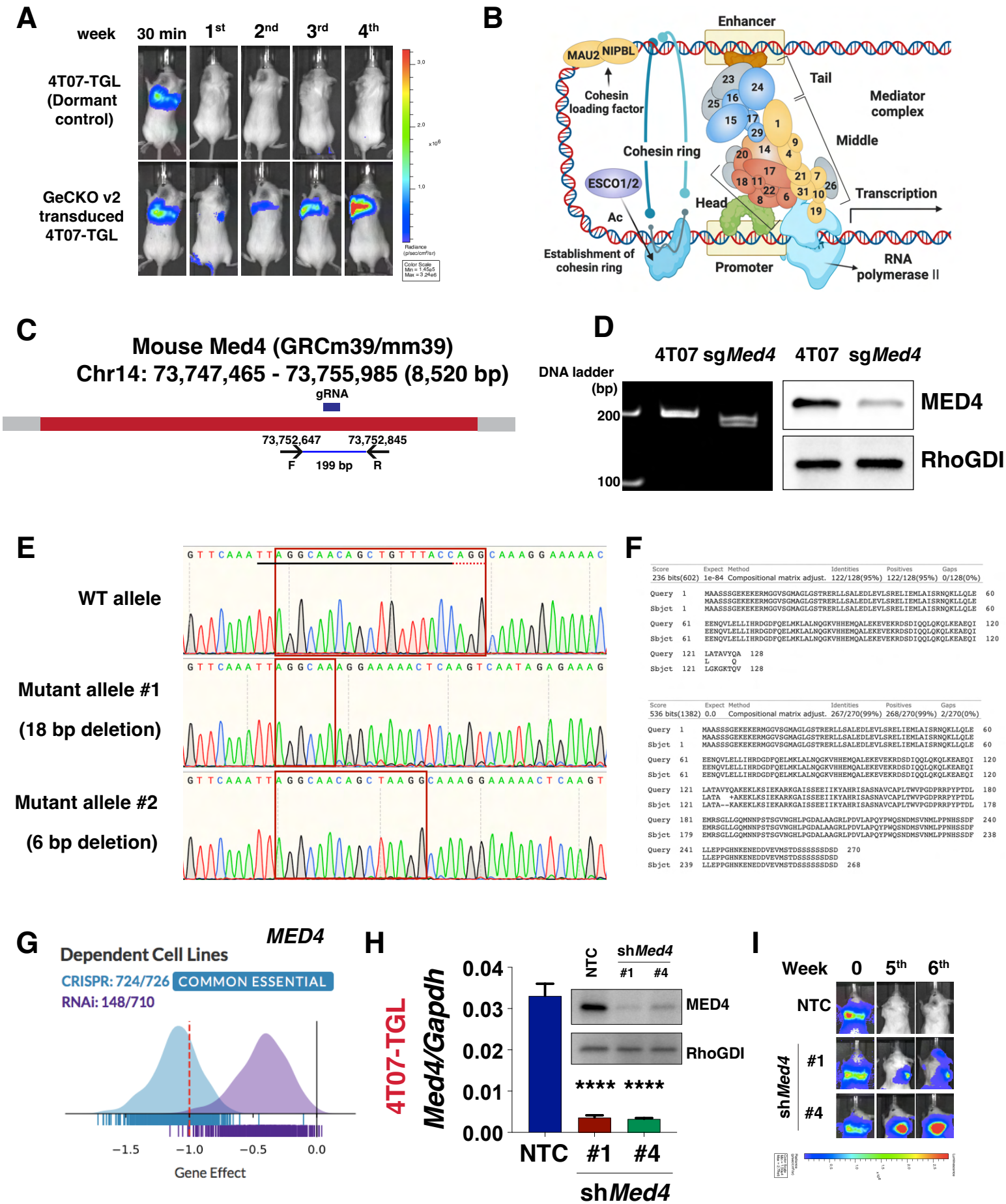

Figure S2 Bae et al.

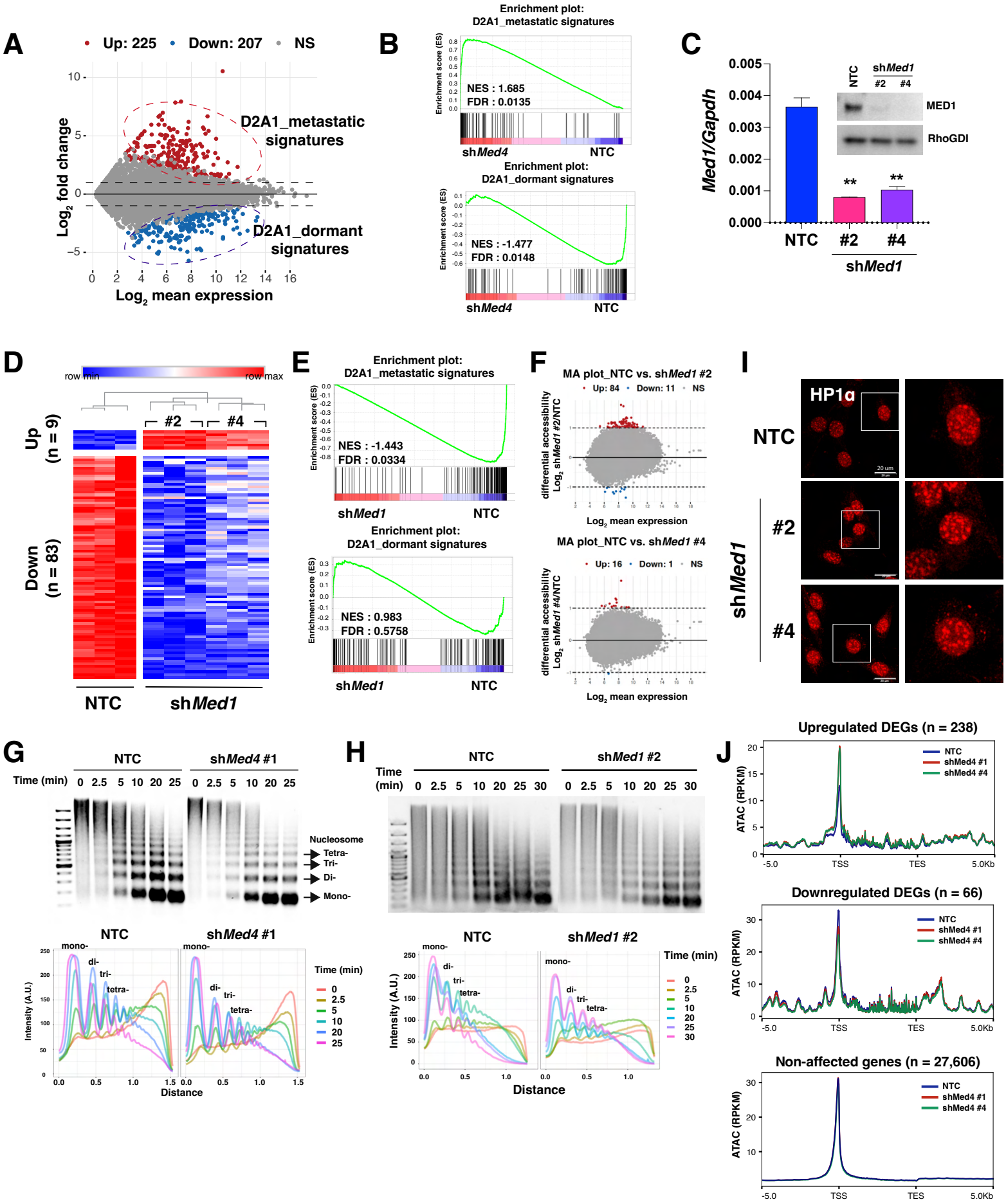

Figure S3 Bae et al.

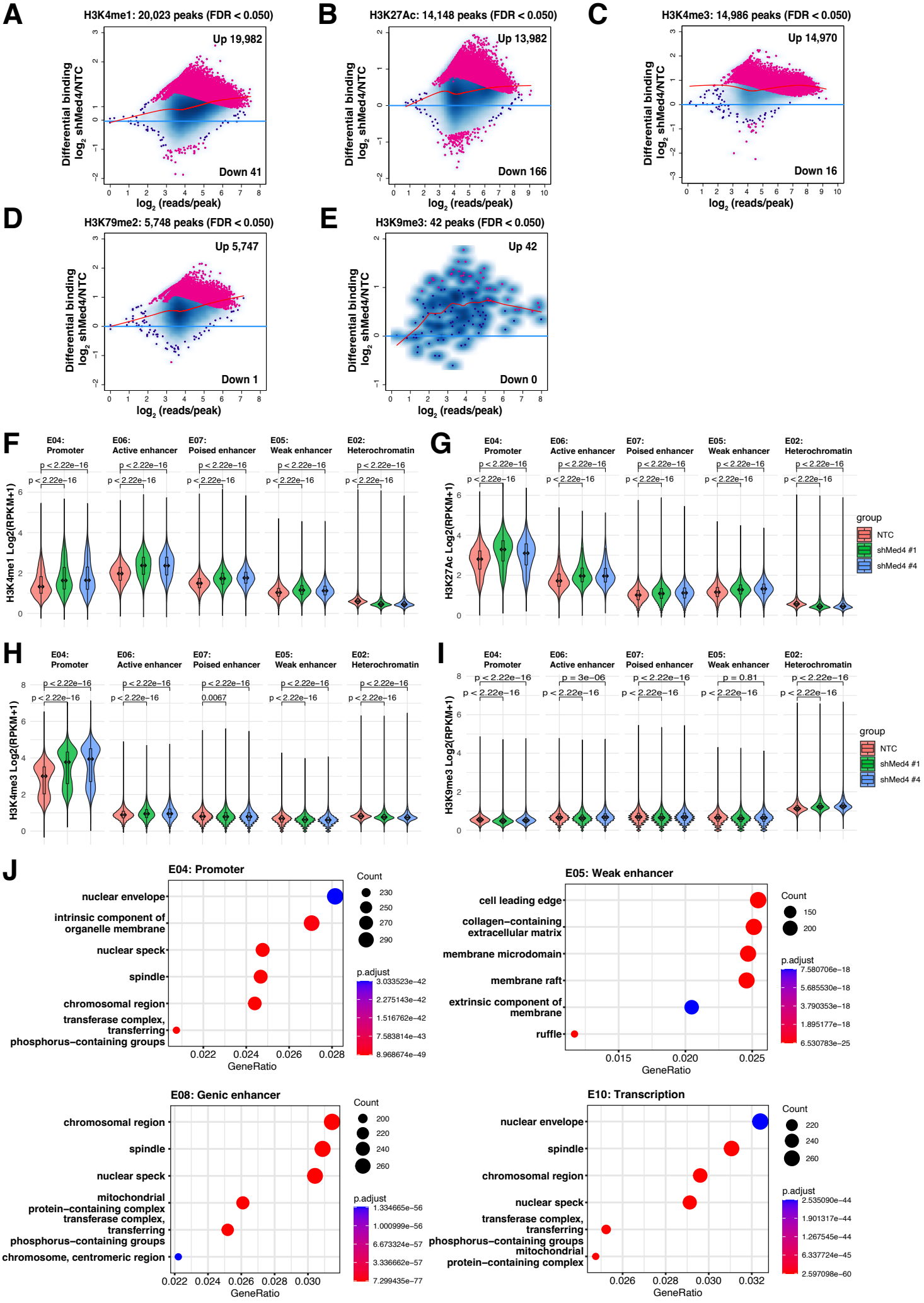

Figure S4 Bae et al.

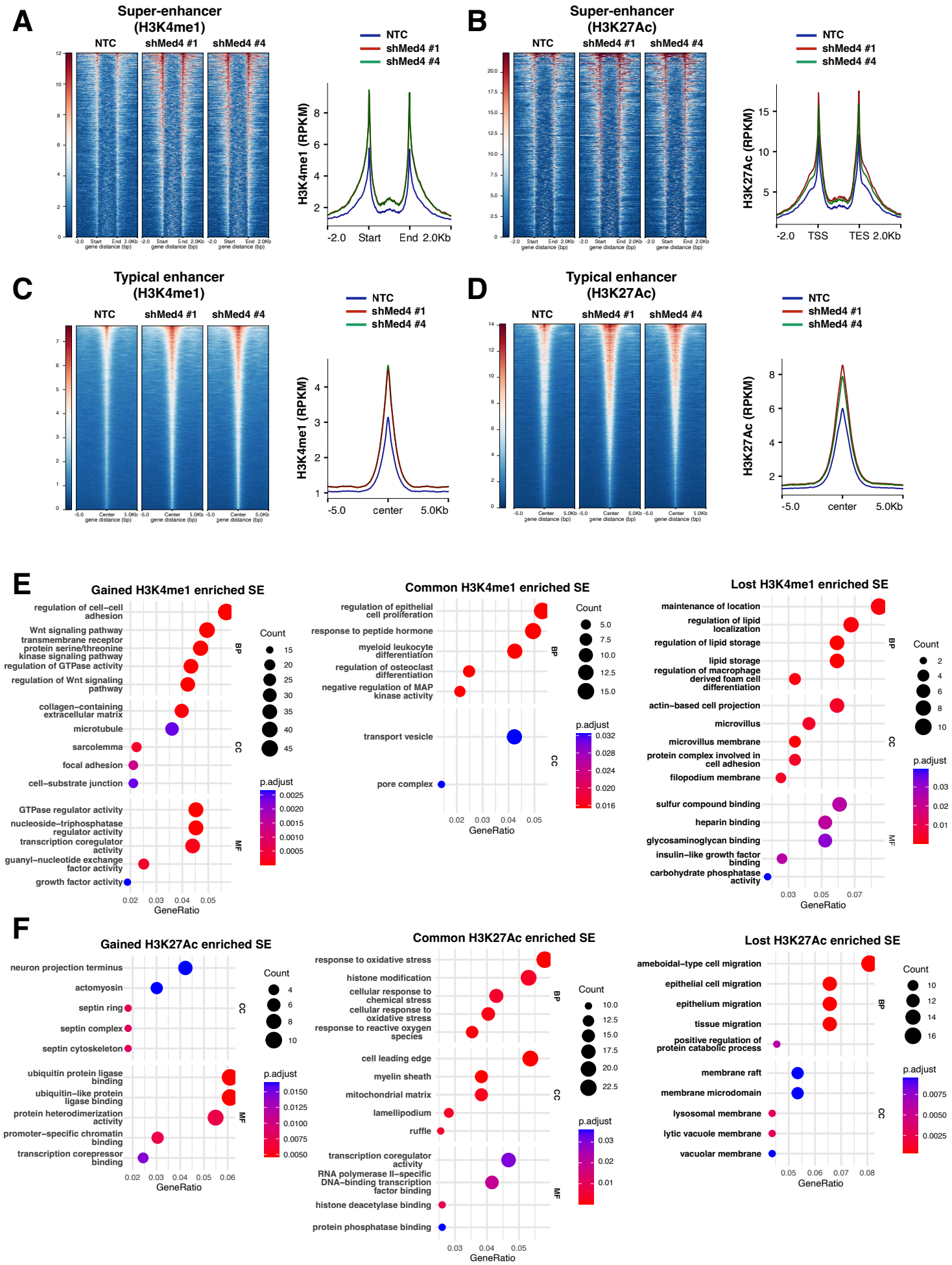

Figure S5 Bae et al.

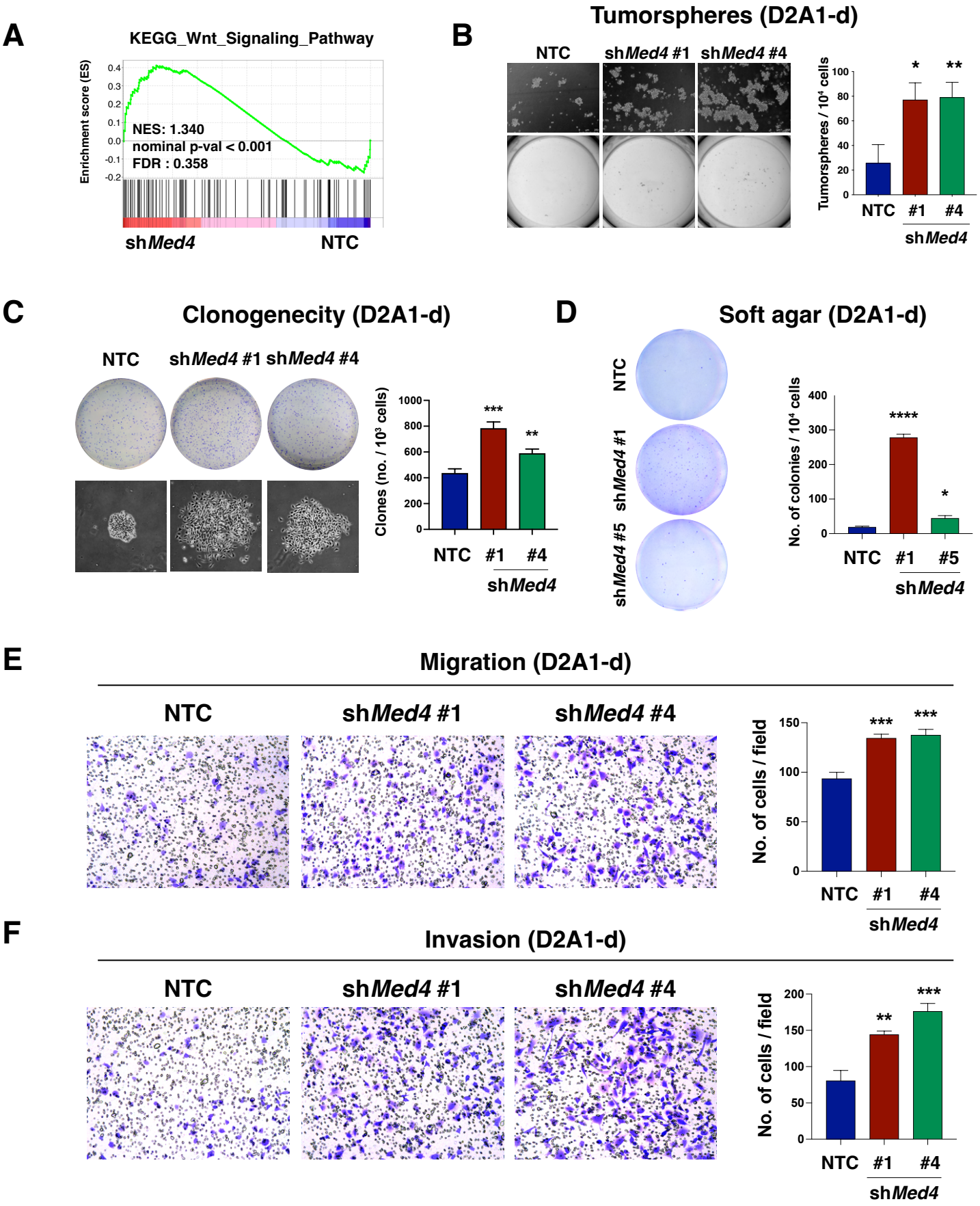

Figure S6 Bae et al.

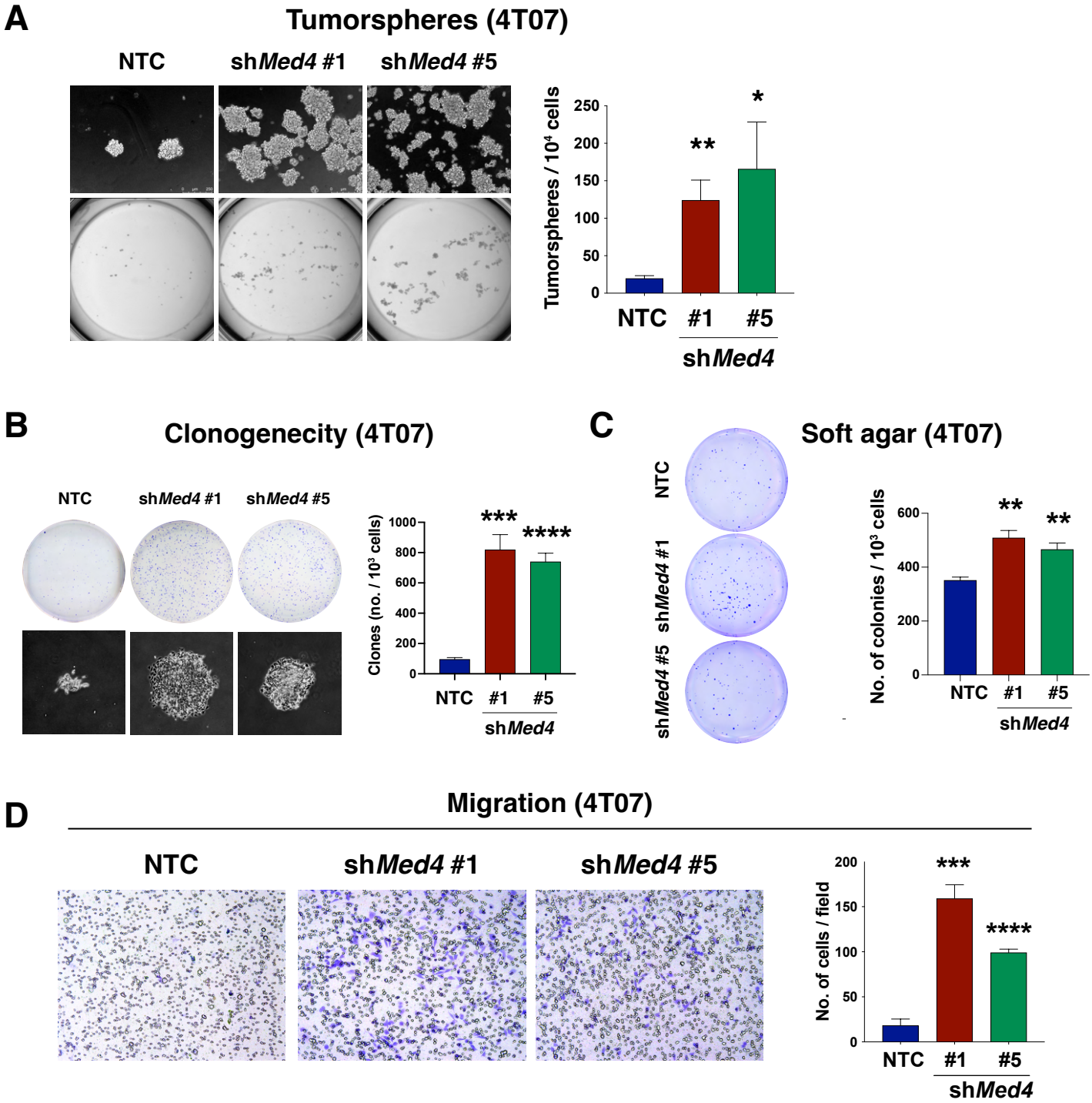

Figure S7 Bae et al.

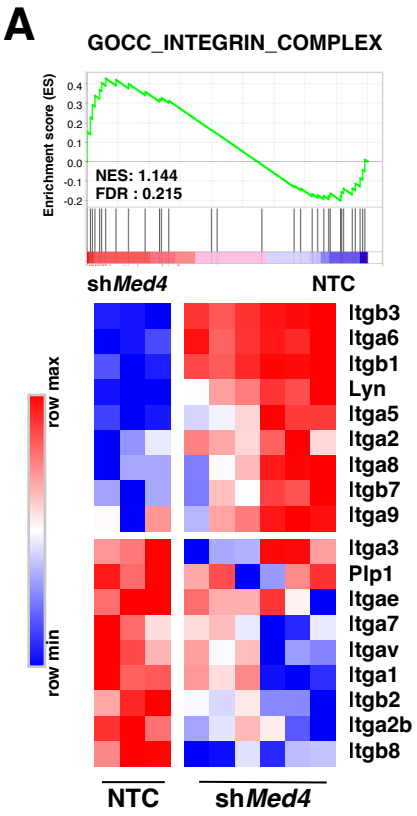

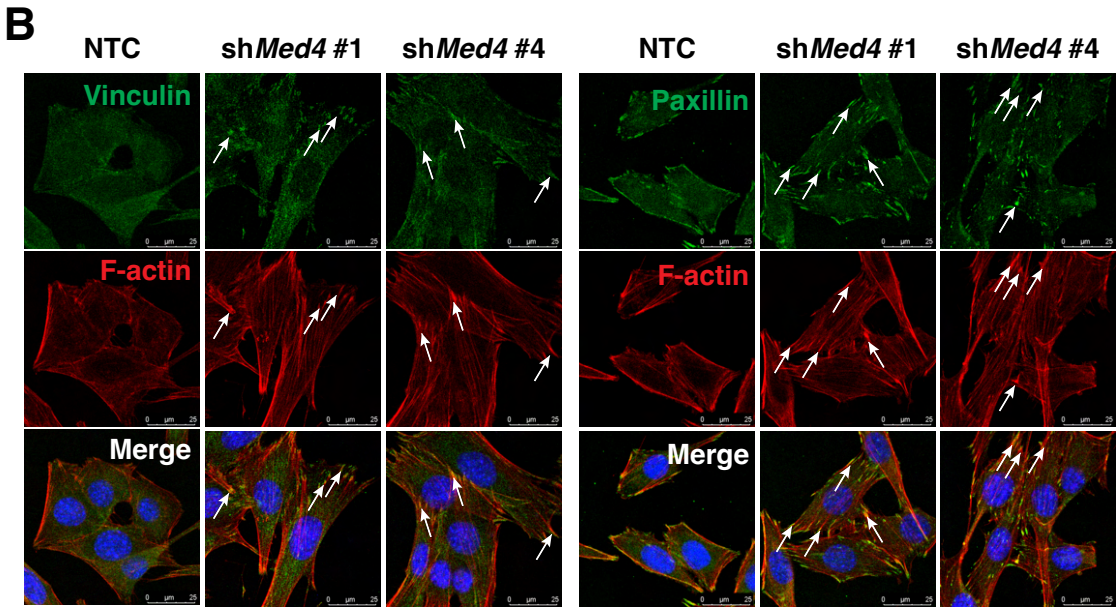

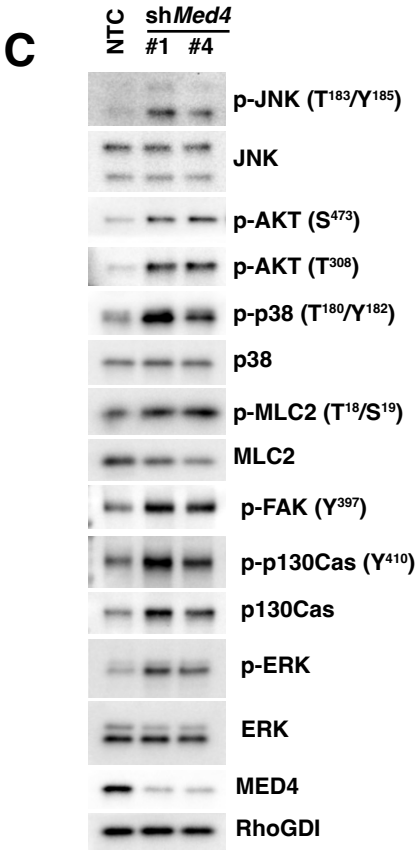

Figure S8 Bae et al.

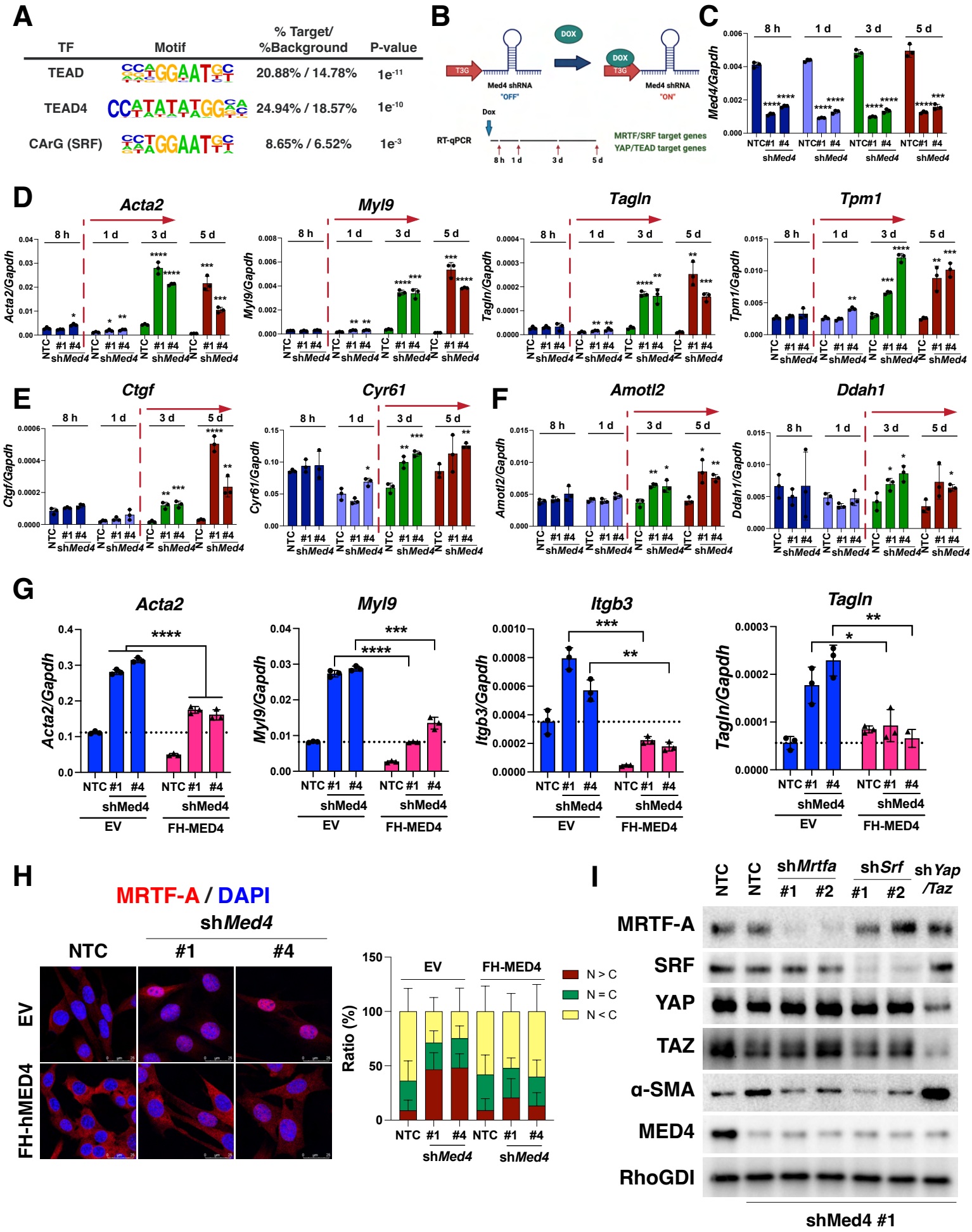
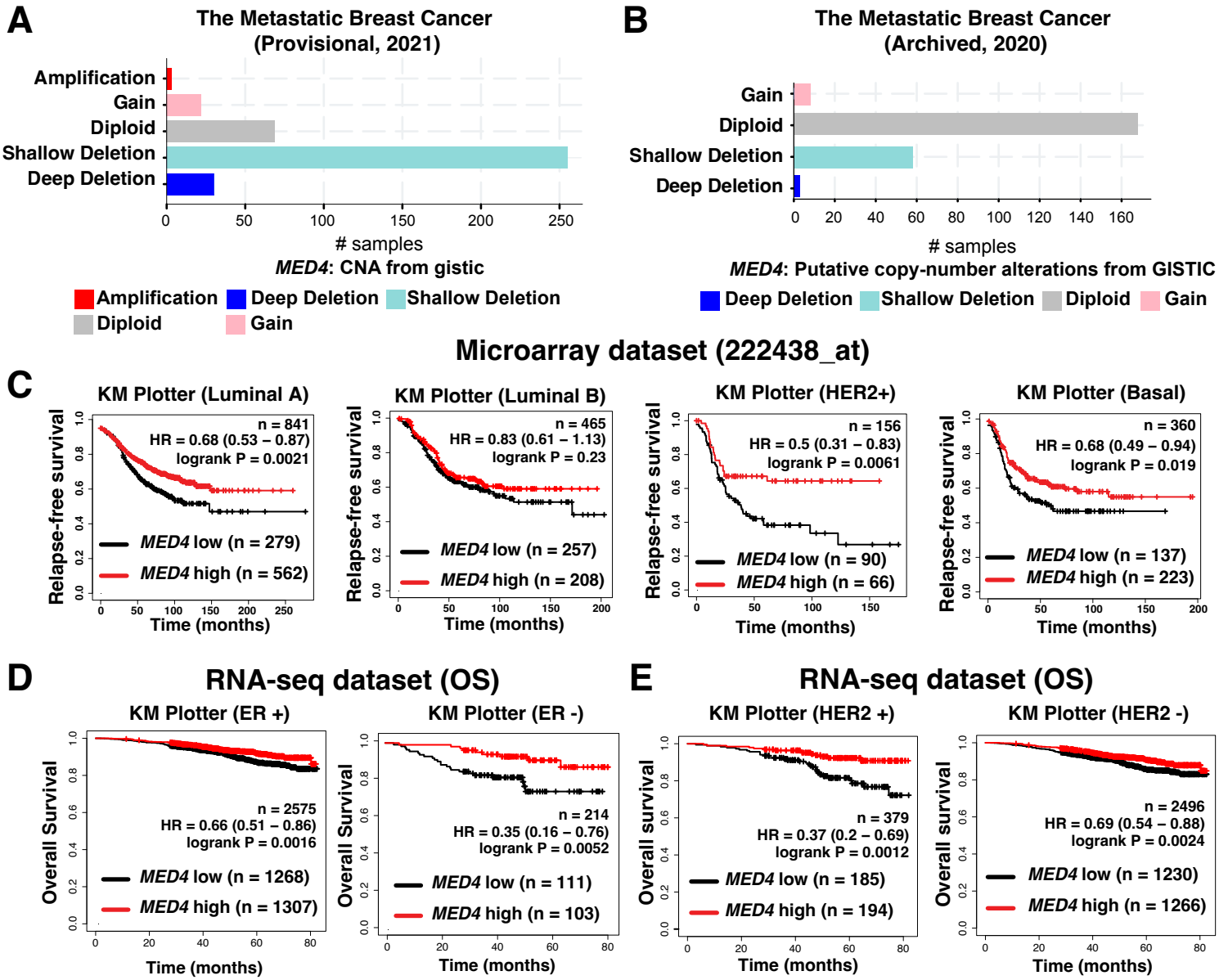
Figure S9 Bae et al.